

A 2MASS Analysis of the Stability of Southern Bok Globules¹

Germán A. Racca and José W. S. Vilas-Boas

INPE-DAS, Av. dos Astronautas 1758, Jardim da Granja, 12227-010, São José dos Campos-SP, Brazil.

german@das.inpe.br, jboas@das.inpe.br

and

Ramiro de la Reza

Observatório Nacional, Rua General José Cristino 77, São Cristóvão, 20921-400, Rio de Janeiro, Brazil.

delareza@on.br

ABSTRACT

We used near-infrared 2MASS data to construct visual extinction maps of a sample of Southern Bok globules utilizing the NICE method. We derived radial extinction profiles of dense cores identified in the globules and analyzed their stability against gravitational collapse with isothermal Bonnor-Ebert spheres. The frequency distribution of the stability parameter (ξ_{max}) of these cores shows that a large number of them are located in stable states, followed by an abrupt decrease of cores in unstable states. This decrease is steeper for globules with associated IRAS point sources than for starless globules. Moreover, globules in stable states have a Bonnor-Ebert temperature of $T = 15 \pm 6$ K, while the group of critical plus unstable globules has a different temperature of $T = 10 \pm 3$ K. Distances were estimated to all the globules studied in this work and the spectral class of the IRAS sources was calculated. No variations were found in the stability parameters of the cores and the spectral class of their associated IRAS sources. On the basis of ^{13}CO $J = 1-0$ molecular line observations, we identified and modeled a blue-assymmetric line profile toward a globule of the sample, obtaining an upper limit infall speed of 0.25 km s^{-1} .

Subject headings: dust, extinction — infrared: ISM — ISM: globules — stars: formation

¹Based on a Ph.D. Thesis made at Observatório Nacional, Rio de Janeiro, Brazil.

1. Introduction

Bok & Reilly (1947) were the first to call attention to small dark regions, dense and rounded, which called *globules*, and suggested the possibility that the star formation could occur within them. These objects were called later Bok globules and in general they are isolated, cold ($T \sim 10$ K), dense ($n \sim 10^{4-5} \text{ cm}^{-3}$), and seen as potential sites for the formation of low-mass stars ($< 10 M_{\odot}$). Following Beichman et al. (1986), the globules that do not contain protostars or young stellar objects (YSOs) associated, are called starless cores. When they show some evidence of star formation, such as Class 0 or I protostars, are called protostellar-cores (André et al. 1993).

As the majority of the stars form in molecular cloud complexes and in clusters embedded in giant molecular clouds and not in isolation, it is very important to know in detail the physical processes that give rise to the formation of a single star in an isolated environment. For this purpose, Bok globules constitute an ideal laboratory to study the isolated low-mass star formation (Bourke et al. 1995a, hereafter BHR).

Visual extinction was used by Clemens & Barvainis (1988) to study 248 Bok globules in the Northern Hemisphere, and by BHR to study 169 globules in the Southern Hemisphere. Sub-millimeter and millimeter wavelength studies of starless cores (Ward-Thompson et al. 1994), indicate that the 1D profiles (mean of azimuthal distributions) are flat for radii $\sim 3000-7000$ AU, and steeper for larger radii. These profiles deviate from the distribution $n(r) \propto r^{-2}$ of the singular isothermal sphere, proposed by Shu (1977) as the initial state of isolated dense cores before gravitational collapse. Similar profiles are obtained by mapping the dust distribution in a dense core or Bok globule. These configurations are consistent with “Bonnor-Ebert spheres” (Ebert 1955; Bonnor 1956), which are non-singular solutions to the equations of hydrostatic equilibrium confined by an external pressure. In the 1D isothermal approximation, there is a family of Bonnor-Ebert solutions parametrized by the central density n_c , where the density profile is characterized by two regimes: a slow decrease in the density for small radii, and a faster decrease, of power-law type ($\propto r^{-2}$), for larger radii.

Detailed modelling of profiles in the infrared (Kandori et al. 2005; Teixeira et al. 2005) and continuum emission (e.g., Ward-Thompson et al. 1999) confirm that Bonnor-Ebert spheres are a good approach to the internal structure of starless cores. However, it is not currently possible to distinguish between a static Bonnor-Ebert sphere and a collapsing one for profiles based in dust absorption or emission, since the structure of the profile, for a given n_c , does not change significantly until the last stages of collapse (Myers 2005).

Using near-infrared observations, Alves et al. (2001) showed that a Bonnor-Ebert sphere

with stability parameter $\xi_{max} = 6.9$ adjust perfectly the observed column density profile of the starless globule Barnard 68. Harvey et al. (2001) modeled the profile of the protostellar globule B335 with $\xi_{max} = 12.5$, and Harvey et al. (2003) estimated $\xi_{max} = 25$ for the starless core L694-2. The Coalsack globule 2 was modeled by Racca et al. (2002) that derived $\xi_{max} = 7.3$, while Lada et al. (2004) obtained $\xi_{max} = 5.8$ using a more sensitive telescope. In recent works, Huard et al. (2006) found $\xi_{max} = 35.8$ for the protostellar core L1014, and Kainulainen et al. (2007) obtained $\xi_{max} = 23$ for the protostellar globule DCld303.8-14.2 and $\xi_{max} \gtrsim 8$ for the starless globule Thumbprint Nebula.

The largest sample of Bok globules studied in the near-infrared was done by Kandori et al. (2005) where 14 globules were selected. They found that more than half of the starless globules (7 out of 11) are located close to the critical state, with $\xi_{max} = 6.5 \pm 2$. This led Kandori et al. (2005) to suggest that a Bonnor-Ebert sphere in the critical state characterizes the structure of typical starless cores. The remaining starless globules and those that present evidence of star formation show clearly unstable states, with $\xi_{max} > 10$.

In this work, we present a study of 21 Southern Bok globules, where 11 are starless and 10 have associated IRAS¹ point sources. In §2 we present the source list and the observations. Using 2MASS data, we constructed visual extinction maps in §3, which enabled us to detect dense cores embedded in the globules. In §4 we estimated new distances to the globules, and by means of the Bonnor-Ebert model, in §5 we studied their internal structure and stability against gravitational collapse. In §6 we analyzed the IRAS point sources associated to the globules and in §7 we found evidence of infall motions in a globule using millimetric observations of the ¹³CO and C¹⁸O molecules. Our main conclusions are summarized in §8.

2. Observations

2.1. Sample List

In this work, we searched for a list of Bok globules satisfying the following conditions:

1. that they were completely isolated, i.e., neither associated to bright nebula nor to a molecular complex,
2. that they had a distance determination,

¹Infrared Astronomical Satellite (Neugebauer et al. 1984)

Using these criteria, we got 21 Southern Bok globules, selected among 169 globules of the BHR sample, where 11 do not present any evidence of star formation, and 10 have associated IRAS point sources. Following previous definitions (see §1), in the first group there are “starless globules”, and in the second there are “IRAS globules”.

Table 1 presents the selected objects. Column 1 and 2 show the names of the globules as they appear in BHR and Hartley et al. (1986), respectively; columns 3 and 4 give their equatorial coordinates; column 5 shows the optical sizes in arcmins, and column 6 gives the distances determined by BHR.

2.2. Near-Infrared Data

The near-infrared data were obtained from the Two-Micron All Sky Survey (2MASS) catalog (Skrutskie et al. 2006). The 2MASS Point Source Catalog (PSC) contains 471 million stars, covering 99.998 % of the sky in the J($1.24 \mu\text{m}$), H($1.66 \mu\text{m}$) and K_s ($2.16 \mu\text{m}$)² bands, observed with two telescopes of 1.3 meters diameter, located in Mount Hopkins (Arizona, USA) and Cerro Tololo (Chile). The 2MASS PSC is more than 99% complete for $J < 15.8$, $H < 15.1$ and $K < 14.3$.

For each of the globules in Table 1, we retrieved JHK magnitudes and their corresponding uncertainties in the 2MASS PSC in regions of $15' \times 15'$ centered on the globules. Only those stars whose photometric uncertainties were ≤ 0.1 mag in all three bands were extracted, ensuring a signal-to-noise ratio $S/N \geq 10$. The search for stars in the 2MASS PSC was made through the web interface Gator³.

2.3. Molecular Line Data

We searched for molecular lines observed toward these globules having line profiles data available. We found only ^{13}CO and C^{18}O ($J = 1-0$) line observations toward the globules BHR 138 and BHR 149 made in 1992 October and 1993 May (see Vilas-Boas et al. 1994). These observations were made with the 15 m Swedish-ESO Submillimeter Telescope (SEST) at La Silla, Chile. The receiver front end was based on a Schottky diode waveguide mixer followed by an intermediate-frequency amplifier. The SSB system temperature was typically

²From hereafter, filter “ K_s ” will be called simply “K”.

³ <http://irsa.ipac.caltech.edu/applications/Gator/>

Table 1. Sample List

Name	DC No.	R.A. (J2000)	Dec. (J2000)	Size ($a' \times b'$)	Distance (pc)
Starless Globules					
016	255.4-3.9	08 05 26	−39 08 54	6×2	300
044	269.5+4.0	09 26 19	−45 11 00	2×2	300
053	274.2-0.4	09 28 47	−51 36 42	8×4	500
059	291.1-1.7	11 07 07	−62 05 48	5×3	250
074	300.0-3.7	12 22 09	−66 27 06	3×3	175
075	300.2-3.5	12 24 13	−66 10 42	6×3	175
111	327.2+1.8	15 42 20	−52 49 06	3×2	250
113	331.0-0.7	16 12 43	−52 15 36	8×4	200
133	340.5+0.5	16 46 45	−44 30 48	10×4	700
144	346.4+7.9	16 37 28	−35 13 54	7×1	170
145	347.5-8.0	17 48 01	−43 43 12	8×5	450
IRAS Globules					
034	267.2-7.2	08 26 34	−50 39 54	8×2	400
058	289.3-2.8	10 49 00	−62 23 06	5×3	250
117	334.6+4.6	16 06 18	−45 55 18	7×2	250
121	337.1-4.9	16 58 42	−50 35 48	2×2	300
126	338.6+9.5	16 04 29	−39 37 48	6×5	170
138	345.0-3.5	17 19 36	−43 27 06	10×6	400
139	345.2-3.6	17 20 45	−43 20 30	4×2	400
140	345.4-4.0	17 22 55	−43 22 36	6×3	400
148	349.0+3.0	17 04 26	−36 18 48	2.5×2.5	200
149	349.2+3.1	17 04 27	−36 08 24	3×1	200

Note. — Units of right ascension are hours, minutes, and seconds, and units of declination are degrees, arcminutes, and arcseconds.

390 K.

The back end used an acousto-optical spectrometer with resolution 43 kHz (0.11 km s⁻¹) and total bandwidth of 100 MHz. The spectra were taken by using overlap frequency switching mode (with 7 MHz frequency shift) and integrating, on average, for periods of 2 minutes. The observations were chopped against a cold load to obtain the correction for atmospheric attenuation. The halfpower beam width was 48'' and the beam efficiency 0.9. The rms pointing accuracy was better than 10''.

3. Visual Extinction Maps

We used the NICE method of Lada et al. (1994) to construct visual extinction maps for the globules. This technique uses a control field region free of reddening to refer the extinctions measured in the cloud region, and assumes that the stellar population is the same in the control field and the cloud region. If we know the intrinsic color of a star, then the color excess is:

$$E(H - K) = (H - K)_{observed} - (H - K)_{intrinsic}. \quad (1)$$

Intrinsic $(H - K)$ colors for main-sequence and giant stars are in a small interval, 0.0 to 0.3 for stars with spectral types between A0 and M5-7 (Koornneef 1983; Bessell & Brett 1988). Therefore, we can approximate the intrinsic color of each on-cloud star by the average color of the control field, and the color excess is:

$$E(H - K) = (H - K) - \overline{(H - K)}_{control}. \quad (2)$$

Using equation 2, we calculate the color excess for each star in the globule region. Then, we can express this color excess in terms of visual extinction with the knowledge of the reddening law in the 2MASS system. Following Nielbock & Chini (2005), this relation is:

$$A_V = 19.4 \times E(H - K), \quad (3)$$

whose associated uncertainty is:

$$\sigma_{A_V} = 19.4 \times \sqrt{\sigma_i^2 + \sigma_{control}^2}, \quad (4)$$

where σ_i is the uncertainty in the observed ($H-K$) color and $\sigma_{control}$ is the standard deviation of the colors in the control field. Nearly 90% of the regions have $\sigma_{control} \sim 0.1$ mag, which sets the minimum measurable value for the extinction in ~ 2 mag. Only two regions in our sample have $\sigma_{control} \sim 0.2$ mag, giving a minimum of ~ 4 mag of visual extinction.

In this way, we obtained the distribution of extinction in the fields containing the Bok globules. However, the spatial distribution of stars is non-uniform. In order to produce a uniformly sampled extinction map, we smoothed the data by spatially convolving the extinction measurements (equation 3) with a Gaussian filter (kernel) with a given smoothing parameter (resolution), and finally sampled the map at the Nyquist frequency (e.g., Lada et al. 1999). The form of the Gaussian kernel is given by:

$$K(\alpha, \alpha_i, \delta, \delta_i) = \frac{1}{2\pi} \exp\left(-\frac{r_i^2}{2h^2}\right), \quad (5)$$

where

$$r_i^2 = (\delta - \delta_i)^2 + (\alpha - \alpha_i)^2 \cos^2(\delta), \quad (6)$$

and h is the map resolution. Hence, the visual extinction A_V at each point (α, δ) in the map is calculated using:

$$A_V(\alpha, \delta) = \frac{\sum_{i=1}^n K(\alpha, \alpha_i, \delta, \delta_i) \times A_V(\alpha_i, \delta_i)}{\sum_{i=1}^n K(\alpha, \alpha_i, \delta, \delta_i)}, \quad (7)$$

where n is the total number of stars observed in the cloud region and $A_V(\alpha_i, \delta_i)$ is given by equation 3, and the associated uncertainty for the extinction at the point (α, δ) in the map is (Lombardi & Alves 2001):

$$\sigma_{A_V}(\alpha, \delta) = \sqrt{\frac{\sum_{i=1}^n K^2(\alpha, \alpha_i, \delta, \delta_i) \times \sigma_{A_V}^2(\alpha_i, \delta_i)}{\sum_{i=1}^n K^2(\alpha, \alpha_i, \delta, \delta_i)}}, \quad (8)$$

where $\sigma_{A_V}(\alpha_i, \delta_i)$ is given by equation 4.

3.1. Construction of the Extinction Maps

To test the 2MASS data using the NICE method, we applied it to Barnard 68 (B68), a well known and studied Bok globule. Alves et al. (2001) observed B68 with the ESO-NTT

telescope in the JHK bands to produce an extinction map of this globule with a resolution of $10''$.

The choice of the smoothing parameter h is a compromise between a final map with high signal-to-noise ratio and low spatial resolution, or a noisy map with high resolution (Lombardi & Alves 2001). To construct the extinction map of B68 (and all the globules in this work) we choose $h = 20''$. Nonetheless, other values were tested: with $h = 10''$ the map is very noisy, and with $h = 30''$ the map loses details. Therefore, a choice of $h = 20''$ provides the best spatial resolution for a signal-to-noise ratio between 8 and 12 in the central region of B68. Figure 1 shows the visual extinction map for B68 constructed using data from the 2MASS catalog. Comparing with the map of Alves et al. (2001), we see a good correspondence between them, taking into account that the 2MASS used a 1.3 meters telescope, while Alves et al. used a 3.5 meters telescope and longer integration times. The sensitivity difference between these telescopes is certainly responsible for the different values of extinction found in the center of B68. From the 2MASS data, we obtain a maximum extinction of 24 magnitudes, while Alves et al. (2001) and Hotzel et al. (2002b), using the same data set, derived 30 magnitudes. This result shows that the extinctions derived toward the center of the globules in our sample, as well as the density contrast, have to be seen as lower limits. In despite of getting a lower extinction peak, the extinction distribution and the peak position are coincident.

Figure 2 shows the visual extinction maps for all Bok globules in our sample. They were constructed with the NICE method as described in §3. Each map has $\sim 15' \times 15'$, centered on the position listed in Table 1. In the right side of each map, a bar indicates the extinction in magnitudes. White crosses superimposed denote the IRAS sources associated to the globules (see §6).

3.2. Comparison with the Star Counts Method

In this item we compare star counts and the NICE methods in order to verify which one is more appropriate to study extinction toward the Bok globules of our sample, derived from 2MASS data.

The 2MASS maps constructed in this work were performed only with those stars whose color excess $E(H - K) > 0$, thus removing almost all foreground stars that can be present in each globule region. This allowed us to minimize the effects that foreground stars can produce in the construction of the extinction maps (see Figure 6 of Cambrésy et al. 2002).

In order to test if the 2MASS data together with the NICE method can produce reliable

dust extinction maps of Bok globules, we also constructed maps using the traditional star counts method. The number of stars per unit area brighter than m_λ in the control field, N_{off} , is:

$$\log(N_{off}) = a + bm_\lambda. \quad (9)$$

On the cloud region, the slope of equation 9 remains the same, but the number of stars per unit area, N_{on} , decreases as extinction increases. The extinction is then:

$$A_\lambda = \frac{1}{b} \log \left(\frac{N_{off}}{N_{on}} \right), \quad (10)$$

where b is the slope of the cumulative luminosity function (see, e.g., Gregorio Hetem et al. 1988). We converted the A_λ extinction (with $\lambda = J, H, K$) to optical A_V extinction using the reddening law in the 2MASS system (Nielbock & Chini 2005).

We constructed extinction maps for B68, our test globule, and for BHR 059, one of the smallest globules in our sample, using the star counts technique with the condition that, at least, one star must be present in each counting box. We obtained three Nyquist sampled maps for each globule, that is, one map for counts in J, H and K bands, respectively. Table 2 shows the parameters used in equation 10 to build the maps.

The extinction maps for B68 and BHR 059 are shown in Figure 3. We can see that B68 is not detected in the map based on K band star counts. This is probably because the distribution of the stars in the K band is almost uniform in the most opaque region of B68. The H and J band maps show B68 as a region of extent ~ 3 -4 pixels without any details on

Table 2. Parameters of the Star Counts Maps

Wavelength	Barnard 68			BHR 059		
	Bin	N_{off}	b	Bin	N_{off}	b
J	80''	21	0.36 ± 0.03	70''	16	0.35 ± 0.02
H	50''	8	0.35 ± 0.03	70''	15	0.34 ± 0.01
K	50''	7	0.37 ± 0.02	70''	13	0.32 ± 0.01

the distribution of dust extinction in the core. It is important to note that a non uniform distribution of field stars causes unrealistic peaks of high visual extinction, which are not seen in the DSS red plates. The same situation occurs for BHR 059.

We estimated the errors in the derived visual extinctions (Dickman 1978) and obtained $\delta A_V \sim 4, 8$ and 12 magnitudes for J, H and K band maps, respectively, in regions where $A_V = 0$ (where $N_{on} = N_{off}$) and $\delta A_V \sim 10, 20$ and 30 magnitudes for J, H and K band maps, respectively, in the most opaque regions (where $N_{on} = 1$ in a single counting box). On the other hand, the signal-to-noise ratio for the maps constructed through the NICE method is always greater than 3 in the most extinguished regions where we constructed the radial extinction profiles. Even though the signal-to-noise ratio is not as good for the more diffuse, low extinction regions, it is not crucial for our purposes, because we are interested in the profile of the core embedded in the globule to finally model it with a Bonnor-Ebert sphere. This discussion demonstrates that, to our purposes, the NICE method applied to the 2MASS data is the best way to construct visual extinction maps and trace Bok globules to finally apply the stability analysis of the radial profile.

4. Distance Determination

The knowledge of the distances to the globules is extremely important, as they are necessary to determine several fundamental parameters, such as mass, size, density and also to calculate the luminosities of the young objects embedded in the globules. Several methods have been used to determine distances, being the more typical the star count method (Bok & Bok 1941) and the Wolf diagram (Wolf 1923). A newer technique, proposed by Maheswar et al. (2004), uses optical and near-infrared broadband photometry of stars in the field of the cloud.

In this paper, we employ the technique of Dickman & Clemens (1983), which uses the plot of color excess $E(B - V)$ versus the distance to stars in the vicinity of the cloud. In this graph, a jump in the reddening indicates the presence of a cloud or a group of clouds. The same method was used by BHR to estimate the distance to some globules. However, for the reasons described in §4.1, we decided to calculate ourselves these distances again.

4.1. Application of the Method

To estimate the distances to the Bok globules, we need to know the reddening $E(B - V)$ of the stars in a given area around each globule. Dickman & Clemens (1983) used a region

of $11^\circ \times 16^\circ$ in their work. BHR used circular regions of 5° radius. If the region had not a sufficient amount of stars, they increased the radius to 7.5° or 10° . In this work, we used the SKY2000 catalog of Myers et al. (2002), which has information for $\sim 300,000$ stars brighter than 8 magnitudes, and searched for stars in circles of 3° radius centered on each Bok globule. Figure 4 shows the galactic distribution of the globules, and the circles are their neighborhood used to determine the distance. As we see, some regions coincide, given the proximity between the globules. In these cases, both are assumed to be at the same distance.

To calculate the color excess $E(B - V)$ for each star, we searched the SKY2000 catalog for all those stars with known spectral types, apparent visual magnitude V , and observed color index $(B - V)$. Having the spectral type of a star, we know the absolute magnitude M_V and the intrinsic color index $(B - V)_0$ using the calibration of Schmidt-Kaler (1982). Assuming a value of 3.1 for the total-to-selective extinction ratio (Rieke & Lebofsky 1985), we calculate the extinction along the line of sight of a star in the neighborhood of a globule as:

$$A_V = 3.1 \times E(B - V) = 3.1 \times [(B - V) - (B - V)_0], \quad (11)$$

and finally the distance in parsecs, corrected for extinction:

$$\log(r) = \frac{1}{5}(V - M_V + 5 - A_V). \quad (12)$$

Figure 5 shows the graphics of $E(B - V)$ versus distance for the globules, where the dashed lines indicate the distances adopted here. In Table 3, column 1 indicates the BHR globule name, column 2 the distance obtained in this work, and column 3 the distance obtained by BHR.

5. Internal Structure: Bonnor-Ebert Models

To study the internal structure of the Bok globules, they were fitted with Bonnor-Ebert isothermal spheres. From the extinction maps generated in §3, radial extinction profiles were built for all the Bok globules considered here.

A sphere of self-gravitating gas in hydrostatic equilibrium, where the pressure and density at each point are related through the isothermal equation of state, is called a Bonnor-Ebert sphere (Ebert 1955; Bonnor 1956). Bonnor (1956) studied the gravitational stability of

Table 3. Distances to the Bok Globules

Name	Distance ^a (pc)	Distance ^b (pc)
016	250	300
034	200	400
044	200	300
053	200	500
058	200	250
059	200	250
074	175	175
075	175	175
111	250	250
113	200	200
117	175	250
121	125	300
126	250	170
133	225	700
138	225	400
139	225	400
140	225	400
144	225	170
145	150	450
148	175	200
149	175	200

^aDistance obtained in this work.

^bDistance obtained by Bourke et al. (1995a).

isothermal spheres and deduced a critical parameter that allows classify them as stable or unstable against gravitational collapse.

The shape of a Bonnor-Ebert density profile consists of a flat central region and a steeper external region, of the form $\rho(r) \propto r^{-2}$. For a Bonnor-Ebert sphere with radius R and central density ρ_c , its normalized profile, i.e., $\rho(r)/\rho_c$ vs. r/R , is characterized by a dimensionless radius ξ_{max} , whose critical value is 6.5. This value of the critical parameter corresponds to a contrast between the central density and the density at the edge of the sphere of 14. Increasing values of this parameter denote spheres more centrally condensed.

5.1. Radial Extinction Profiles, Masses and Densities

In order to construct radial profiles, we define the position of the center of the globule as the position of the extinction peak, which does not necessarily coincide with the position listed in Table 1. As some extinction maps have more than one core for the same globule, we will assign a letter to the new cores identified within a single globule. Then, we set concentric annuli at each core center, $20''$ wide, and averaged the extinction at the Nyquist frequency, obtaining a mean extinction value every $10''$ (impact parameters). The resulting uncertainty for an impact parameter corresponds to the error propagation of each pixel within the annulus, calculated with equation 8. The radial profile for B68 is shown in Figure 6, and the resulting radial extinction profiles for the globules of our sample are shown in Figure 7. The solid curve in each plot corresponds to the Bonnor-Ebert fitting (see §5.2).

As shown in §5.2 and §5.3 below, to fit these profiles we modeled a radial density profile for each impact parameter, and the radius R of the core is the impact parameter for which we obtained the best fit for that profile. Teixeira et al. (2005) define the radius of a core as the distance for which the profile reaches a constant level of extinction or *plateau*. The radius obtained in this article coincide with the definition of Teixeira et al. because the cores are embedded in a more diffuse region in the globules. Table 4 lists in column 1 the BHR globules, where a letter attached represents a substructure identified in the globule, columns 2 and 3 give the coordinates of the cores as defined above, and column 4 lists their sizes.

Once constructed the radial profiles of the cores, we calculate their masses integrating the profile until the radius of the core:

$$M = \mu m_H \int_{\Omega} N_H d\Omega, \quad (13)$$

where μ ($= 1.36$) is the mean atomic weight of the gas, m_H is the mass of the H atom, N_H is

Table 4. Coordinates and Sizes of Dense Cores in Bok Globules

Name	R.A. (J2000)	Dec. (J2000)	R (pc)
Starless Globules			
016 A	08 05 18.8	–39 08 53	0.07
016 B	08 05 27.2	–39 08 20	0.06
044 A	09 26 09.3	–45 11 10	0.07
044 B	09 26 20.4	–45 10 56	0.06
053	09 28 46.5	–51 36 20	0.07
059	11 07 10.1	–62 05 36	0.06
074	12 22 10.2	–66 27 39	0.07
075	12 24 14.2	–66 10 58	0.09
111	15 42 19.8	–52 48 26	0.11
113	16 12 51.6	–52 16 23	0.07
133	16 46 42.6	–44 31 10	0.13
144 A	16 37 29.3	–35 13 43	0.07
144 B	16 37 35.5	–35 14 43	0.07
145	17 47 51.9	–43 42 15	0.07
IRAS Globules			
034	08 26 27.7	–50 39 30	0.06
058	10 49 02.4	–62 22 18	0.05
117 A	16 06 25.2	–45 54 17	0.06
117 B	16 06 11.8	–45 56 29	0.06
121	16 58 47.0	–50 36 34	0.06
126	16 04 29.2	–39 37 47	0.11
138	17 19 32.9	–43 26 55	0.10
139	17 20 51.7	–43 19 44	0.07
140 A	17 22 56.2	–43 22 26	0.07
140 B	17 22 52.9	–43 21 40	0.06
140 C	17 23 29.6	–43 25 10	0.06
148	17 04 26.4	–36 18 34	0.07
149 A	17 04 31.2	–36 07 52	0.06
149 B	17 04 53.1	–36 03 15	0.06

Note. — Units of right ascension are hours, minutes, and seconds, and units of declination are degrees, arcminutes, and arcseconds.

the column density and Ω is the cloud area projected in the plane of the sky. To express the column density in terms of visual extinction, we used the gas-to-dust ratio of Bohlin et al. (1978):

$$N_H = 2 \times 10^{21} A_V \text{ cm}^{-2} \text{ mag}^{-1}, \quad (14)$$

and subtracting the contribution of the diffuse structure or *plateau* extinction, we have that the mass of an embedded dense core is:

$$M = 2\pi \left(\frac{N_H}{A_V} \right) \mu m_H D^2 \int_0^R \left(A_V - A_V^{\text{plateau}} \right) r dr, \quad (15)$$

where D is the distance to the globule and R is the core radius. Finally, to calculate the mean volumetric density of each core, we used:

$$\bar{n} = \frac{3M}{4\pi \mu m_H R^3}. \quad (16)$$

The above results are listed in Table 5. Column 1 indicates the core name, column 2 the *plateau* extinction, column 3 and 4 are the masses and mean volumetric densities of the cores without *plateau* subtraction, and in columns 5 and 6 are given the masses and densities subtracting the *plateau* contribution.

5.2. Bonnor-Ebert Model

A Bonnor-Ebert sphere is a pressure-truncated, self-gravitating isothermal sphere of gas in hydrostatic equilibrium. The equation that describes such a gaseous sphere is the modified Lane-Emden equation:

$$\frac{1}{\xi^2} \frac{d}{d\xi} \left(\xi^2 \frac{d\phi}{d\xi} \right) = e^{-\phi}, \quad (17)$$

where $\rho = \rho_c e^{-\phi(\xi)}$. Here, $\xi = (r/a)\sqrt{4\pi G \rho_c}$ is a dimensionless radial parameter and a is the isothermal sound speed. Introducing standard boundary conditions ($\phi(0) = 0$ and $d\phi(0)/d\xi = 0$), we solved equation 17 numerically using a fourth order Runge-Kutta method. Assuming an external radius R , solutions of equation 17 can be parametrized by ρ_c . Bonnor (1956) demonstrated that the value of ξ evaluated at the external radius R :

Table 5. Masses and Densities of Dense Cores in Bok Globules

Name	$A_V^{plateau}$ (mag)	M^a (M_\odot)	\bar{n}^a (10^4 cm^{-3})	M^b (M_\odot)	\bar{n}^b (10^4 cm^{-3})
Starless Globules					
016 A	8.7	9.5	19.1	3.6	7.2
016 B	6.2	4.7	15.1	1.2	3.8
044 A	5.1	5.4	10.9	1.4	2.7
044 B	5.8	4.0	12.9	1.1	3.4
053	7.1	8.0	16.1	2.4	4.9
059	8.1	6.8	21.7	2.6	8.4
074	2.8	3.6	7.4	1.5	3.0
075	3.5	6.3	5.9	1.8	1.7
111	9.8	22.7	11.8	5.5	2.9
113	7.9	7.7	15.5	1.4	2.9
133	7.5	20.4	6.4	3.2	1.0
144 A	11.7	11.5	23.2	2.6	5.3
144 B	11.1	9.4	18.9	2.2	4.4
145	3.6	3.9	7.8	1.4	2.8
IRAS Globules					
034	2.5	2.2	7.0	0.9	2.8
058	5.4	4.4	24.3	2.1	11.4
117 A	8.9	4.9	15.8	0.9	2.8
117 B	8.3	5.9	18.8	0.8	2.7
121	3.1	2.4	7.8	0.7	2.4
126	6.0	13.0	6.8	2.6	1.3
138	1.9	5.0	3.5	2.3	1.6
139	4.8	6.3	12.8	2.7	5.4
140 A	7.9	6.8	13.7	1.6	3.3
140 B	7.7	5.2	16.6	0.9	3.0
140 C	4.5	3.8	12.3	1.4	4.4
148	4.5	4.8	9.8	1.4	2.8
149 A	4.6	4.0	12.8	1.5	4.9
149 B	3.6	2.8	8.9	0.9	2.8

^aValue without *plateau* subtraction.

^bValue with *plateau* subtraction.

$$\xi_{max} = \frac{R}{a} \sqrt{4\pi G \rho_c} \quad (18)$$

provides a stability measure. Systems with $\xi_{max} > 6.5$ are unstable to gravitational collapse. Equivalently, the density contrast between the center and the border of the cloud is a function of ξ_{max} :

$$\frac{\rho_c}{\rho_R} = e^{\phi(\xi_{max})}. \quad (19)$$

If $\rho_R = \rho(R)$, and in the critical state $\xi_{max} = 6.5$, then $\rho_c/\rho_R = 14$. Equation 19 shows that, for stable states where $\xi_{max} < 6.5$, the center-to-edge density contrast is lesser than 14.

Finally, knowing the core radius R and the stability parameter ξ_{max} , we can calculate the physical parameters of the sphere, as the central density:

$$\rho_c = \frac{1}{4\pi G} \left(\frac{a\xi_{max}}{R} \right)^2, \quad (20)$$

or the volumetric central density:

$$n_c = \frac{\rho_c}{\mu m_H}, \quad (21)$$

where μ ($= 2.33$) is the molecular weight of the H_2 molecule. The mass of the Bonnor-Ebert sphere is given by:

$$M_{BE} = \frac{1}{\sqrt{4\pi\rho_c}} \left(\frac{a^2}{G} \right)^{3/2} \xi_{max}^2 \left(\frac{d\phi}{d\xi} \right)_{\xi=\xi_{max}}, \quad (22)$$

and the external pressure at the edge:

$$P_{ext} = a^2 \rho_c e^{-\phi(\xi_{max})}. \quad (23)$$

5.3. Bonnor-Ebert Fitting

In order to compare theoretical profiles with observed extinction profiles for each core, we constructed a series of theoretical Bonnor-Ebert profiles in the following way: for various

values of the stability parameter ξ_{max} and temperature T , we obtained the volumetric density $n(r)$ solving equation 17 as explained above. Then, we integrated the volumetric density profile along the line-of-sight to obtain the hydrogen column density profile:

$$N_{BE}(r) = 2 \times \int_r^R n(r') \frac{r' dr'}{\sqrt{r'^2 - r^2}}, \quad (24)$$

where r is the projected distance from the center of the core or impact parameter. The stability parameter was varied from 3 to 15 in steps of $\Delta\xi = 0.1$, and the temperature was varied from 5 K to 30 K in steps of $\Delta T = 0.1$ K. To express the column density in terms of visual extinction, we used again the gas-to-dust ratio of Bohlin et al. (1978) given by equation 14. The fitting was evaluated using a reduced χ^2 with 2 degrees of freedom:

$$\chi_r^2 = \frac{1}{n-2} \sum_{i=1}^n \left[\frac{A_V^{BE}(i) - A_V^{obs}(i)}{\sigma_i} \right]^2, \quad (25)$$

where n is the number of points considered in the profile and σ_i is the uncertainty in the observed A_V . To estimate the uncertainty of the best-fit parameters, we took the second derivative of χ_r^2 with respect to each parameter ξ_{max} and T in the region where χ_r^2 is minimum:

$$\sigma_{\xi_{max}}^2 = 2 \left(\frac{\partial^2 \chi_r^2}{\partial \xi_{max}^2} \right)^{-1}, \quad (26a)$$

$$\sigma_T^2 = 2 \left(\frac{\partial^2 \chi_r^2}{\partial T^2} \right)^{-1}, \quad (26b)$$

according to Bevington & Robinson (1992).

The Bonnor-Ebert model applied to B68 using the 2MASS data gave the following results:

$$\xi_{max} = 6.9 \pm 0.3,$$

$$T = 16.8 \pm 0.9 \text{ K}.$$

The theoretical profile for B68 is shown in Figure 6 as a continuous line superimposed on the observed profile. The stability parameter is in good concordance with that obtained by Alves et al. (2001), who calculated $\xi_{max} = 6.9 \pm 0.2$ using a temperature of 16 K measured by Bourke et al. (1995b), which coincides with the value determined in our fit. However, more

recent observations indicate a lower value for the temperature of B68. Hotzel et al. (2002a) observed B68 in NH_3 and obtained a gas kinetic temperature of 10 ± 1.2 K, while Lai et al. (2003) found a value of 11 K using the same molecule. Hotzel et al. (2002b), using the same data, modeled B68 with a Bonnor-Ebert sphere and found central extinctions of $A_V^c = 30.3$ mag, which is different from the value derived in this work, $A_V^c = 19.5$ mag. This difference arises probably because they observed B68 with a greater resolution and sensitivity than the 2MASS, making it possible to detect a larger number of stars toward B68 than 2MASS.

Table 6 summarizes the results of the Bonnor-Ebert modelling for the Bok globules of our sample. Column 1 gives the names of the cores, column 2 the stability parameters, column 3 the Bonnor-Ebert temperatures, column 4 and 5 the central volumetric densities and masses, column 6 the external pressures in units of the Boltzmann constant, column 7 the central extinctions and column 8 the minimum value of χ_r^2 . The resulting theoretical profiles for the globules are shown in Figure 7.

For the physical parameters obtained in the Bonnor-Ebert fitting, we calculated the mean, standard deviation (SD), median, lower quartile (LQ), and upper quartile (UQ) for the whole sample, for the starless globules and for the IRAS globules, respectively. These quantities are shown in Table 7. Comparing starless with IRAS globules, we see from this table that the mean value of the physical parameters are nearly identical for both kind of globules. However, for the temperature and external pressure, starless globules have larger values than IRAS globules. In order to better explore these trends, a large sample of carefully selected globules has to be studied.

It is important to mention that we also used a slightly different fitting procedure, in which the theoretical profile was convolved with a Gaussian kernel of $\text{FWHM} = 20''$, the resolution of the extinction maps. We obtained that, while the temperature remains nearly the same, the stability parameter ξ_{max} seems to be greater in all cases. Nevertheless, their associated uncertainty is also greater for all fittings carried out with kernel convolution, and in more than 60% of the cases the error bars overlap. Also, in all the fittings the reduced χ^2 test is always bigger for convolved profiles, suggesting that there is no need to convolve a theoretical Bonnor-Ebert profile with a Gaussian kernel for fitting the dense cores of our sample using 2MASS data.

5.4. Modelling Results and Discussion

Figure 8 shows the stability parameter ξ_{max} versus the center-to-edge density contrast ρ_c/ρ_R for the globules of our sample. Gray data correspond to starless globules and black

Table 6. Physical Parameters of Dense Cores in Bok Globules from Bonnor-Ebert Fitting

Name	ξ_{max}	T (K)	n_c (10^4 cm^{-3})	M (M_\odot)	P_{ext}/k_B ($10^4 \text{ cm}^{-3} \text{ K}$)	A_V^c (mag)	χ_r^2
Starless Globules							
016 A	5.6 ± 0.1	24.4 ± 1.4	18.8	3.1	46.0	18.2	0.90
016 B	8.2 ± 0.2	8.5 ± 1.2	16.9	1.1	5.6	10.8	0.62
044 A	8.1 ± 0.5	8.3 ± 1.0	11.2	1.2	3.7	8.7	0.45
044 B	3.9 ± 0.7	10.4 ± 1.7	5.1	1.0	11.6	5.6	0.95
053	4.7 ± 0.5	16.6 ± 1.5	7.5	2.1	18.7	9.1	0.61
059	5.3 ± 0.4	21.7 ± 1.2	19.6	2.4	48.6	17.3	1.84
074	6.7 ± 0.5	9.3 ± 1.2	8.7	1.3	5.3	7.9	0.30
075	6.5 ± 1.6	8.5 ± 1.3	4.5	1.6	2.6	5.4	0.08
111	4.9 ± 0.2	25.2 ± 1.8	5.5	4.9	19.0	9.7	0.86
113	6.1 ± 2.0	9.3 ± 2.0	7.1	1.3	5.4	7.0	0.28
133	8.2 ± 0.8	11.0 ± 3.0	5.1	2.8	2.2	6.8	0.06
144 A	4.3 ± 0.1	19.4 ± 1.6	7.7	2.3	27.2	9.7	0.53
144 B	3.4 ± 0.3	20.7 ± 1.7	6.0	1.9	35.6	8.1	0.58
145	5.1 ± 0.3	9.7 ± 1.1	5.7	1.2	6.9	6.2	0.24
IRAS Globules							
034	4.5 ± 0.7	7.9 ± 1.0	5.1	0.8	6.6	5.1	0.72
058	3.8 ± 0.2	22.7 ± 1.3	12.5	1.9	65.8	12.8	3.02
117 A	3.9 ± 0.4	8.9 ± 1.3	4.8	0.8	9.4	5.0	0.27
117 B	3.8 ± 0.3	7.1 ± 1.6	2.7	0.7	4.5	3.4	0.21
121	9.4 ± 0.6	5.1 ± 0.8	13.3	0.6	1.9	7.6	0.46
126	6.8 ± 0.7	10.1 ± 1.9	4.2	2.2	2.7	5.8	0.08
138	6.4 ± 0.4	10.7 ± 1.5	4.9	2.1	3.8	6.3	0.33
139	6.4 ± 0.5	17.6 ± 1.3	15.6	2.5	20.0	14.4	1.95
140 A	4.8 ± 0.7	12.5 ± 1.4	7.3	1.5	13.0	7.8	0.49
140 B	7.0 ± 1.7	7.2 ± 1.1	10.7	0.9	4.5	7.7	0.44
140 C	6.1 ± 0.9	10.7 ± 1.1	12.0	1.3	10.5	9.8	0.97
148	4.0 ± 0.4	10.6 ± 1.8	3.5	1.2	7.8	4.7	0.16
149 A	5.1 ± 0.3	12.7 ± 1.2	10.2	1.4	16.1	9.5	0.75
149 B	6.3 ± 0.6	6.7 ± 1.0	8.2	0.8	4.1	6.4	0.24

Table 7. Statistics for Dense Cores in Bok Globules

Physical Parameter	All Globules					Starless Globules					IRAS Globules				
	Mean	SD	Median	LQ	UQ	Mean	SD	Median	LQ	UQ	Mean	SD	Median	LQ	UQ
R (pc)	0.07	0.02	0.07	0.06	0.07	0.08	0.02	0.07	0.07	0.07	0.07	0.02	0.06	0.06	0.07
ξ_{max}	5.7	1.6	5.5	4.5	6.6	5.8	1.6	5.5	4.8	6.7	5.6	1.6	5.6	4.1	6.4
T (K)	12.6	5.9	10.5	8.5	16.9	14.5	6.5	10.7	9.3	20.4	10.8	4.7	10.4	7.4	12.1
n_c (10^4 cm^{-3})	8.7	4.7	7.4	5.1	11.4	9.2	5.3	7.3	5.6	10.6	8.2	4.2	7.8	4.8	11.7
M (M_\odot)	1.7	0.9	1.4	1.0	2.1	2.0	1.1	1.7	1.3	2.3	1.3	0.6	1.2	0.8	1.8
P_{ext}/k_B ($10^4 \text{ cm}^{-3} \text{ K}$)	14.6	16.2	7.4	4.4	18.8	17.0	16.2	9.3	5.3	25.2	12.2	16.3	7.2	4.2	12.4
A_V^c (mag)	8.5	3.6	7.8	6.1	9.7	9.3	3.9	8.4	6.8	9.7	7.6	3.1	7.0	5.3	9.0

data to IRAS globules. This figure shows that there is no difference between starless and IRAS globules with respect to the stability parameter. Taking into account the uncertainties in ξ_{max} , we can see three groups in this plot: a first group showing clearly stable states, with $\xi_{max} = 4.5 \pm 0.7$ (8 starless + 7 IRAS), a second group distributed around the critical state with $\xi_{max} = 6.5 \pm 0.2$ (3 starless + 6 IRAS), and a third group showing clearly unstable states, with $\xi_{max} = 8.5 \pm 0.6$ (3 starless + 1 IRAS). Remarkably, the first group of stable globules has a temperature of $T = 15 \pm 6$ K, and the critical plus unstable groups have $T = 10 \pm 3$ K. This tendency of decreasing temperature with increasing stability parameter can also be seen in Figure 9, where both parameters are plotted with their respective uncertainties. The same behavior is shown by the external pressure.

These results show a difference with respect to the sample of Kandori et al. (2005): they found that more than half of their starless globules are located near the critical state, which is not our case. Secondly, their Bonnor-Ebert temperature distribution (not shown by these authors) against stability parameter did not show any tendency of decreasing temperature with increasing ξ_{max} , as in our sample.

Figure 10 shows histograms of the logarithmic density contrast, with the vertical dashed line corresponding to the critical Bonnor-Ebert sphere. The left histogram corresponds to the whole sample, showing that there is a large number of cores in the stable regime, followed by an abrupt decrease of cores in the unstable regime. The same behavior is seen for starless globules (upper-right) and for IRAS globules (lower-right), but the decrease in the number of cores for IRAS globules is steeper than for starless globules. This seems to be in agreement with the fact that globules with density contrasts larger than 14 must have shorter lifetimes. The opposite happens when the density contrast is smaller than the critical value. In order to state whether this is a real trend or not a large sample of globules has to be considered. The peak of the starless globules occurs just below the critical value, while for IRAS globules the peak is around the critical value. This is in contrast to the globule distribution showed by Kandori et al. (2005, see their Figure 6), where the majority of starless globules are in the unstable regime and the star-forming globules are well in the unstable regime.

Similarly to Kandori et al. (2005), we plot in Figure 11 the correlations between density contrast and the different parameters of the globules derived from the Bonnor-Ebert fitting in a logarithmic scale. The dotted lines correspond to the variation of each parameter for Bonnor-Ebert spheres with minimum and maximum values of T and P_{ext} ($T_{min} = 5.1$ K and $P_{ext,min} = 1.9 \times 10^4$ cm⁻³ K; $T_{max} = 25.2$ K and $P_{ext,max} = 65.8 \times 10^4$ cm⁻³ K), as indicated in Figures 11 (a) and (b) for the temperature and external pressure, respectively. With these two extreme Bonnor-Ebert spheres, we see in Figures 11 (c)-(f) that we can cover nearly all the points in the plots, which demonstrate that the dispersions in the distributions of the

parameters can be accounted by two Bonnor-Ebert spheres, one with fixed minimum values of T and P_{ext} , and other with fixed maximum values.

Finally, if the IRAS globules are star-forming globules, then our sample of Bok globules do not show an evolutionary sequence, as is the case of Kandori et al. (2005), where their sample of globules suggest an evolutionary sequence in the sense that the starless globules are distributed around a critical Bonnor-Ebert sphere and the star-forming globules are highly unstable.

6. The Infrared Sources

To study the properties the of IRAS sources associated with the globules of our sample, we looked for flux measurements in the following catalogs:

- DENIS⁴ for band I (0.79 μm)
- 2MASS for bands J (1.24 μm), H (1.66 μm) and K (2.16 μm)
- MSX⁵ for bands A (8.28 μm), C (12.13 μm), D (14.65 μm) and E (21.34 μm)
- IRAS for bands 12 μm , 25 μm , 60 μm and 100 μm

To determine the nature of the IRAS sources embedded in the globules, we used two criteria to segregate the spectral classes: in §6.1 we build the spectral energy distribution (SED) for the IRAS sources and calculated the spectral index, and in §6.2 we calculated the bolometric luminosity and temperature for the sources.

6.1. Spectral Energy Distribution

The shape of the broadband spectrum of a YSO depends on the nature and distribution of the circumstellar material. This implies a correlation between the SED and the evolutionary state of the YSO, where the initial protostellar stages, during which a stellar embryo is surrounded by large amounts of collapsing circumstellar material, have very different infrared

⁴Deep Near-Infrared Survey (Epchtein et al. 1999)

⁵Midcourse Space Experiment (Price et al. 2001)

signatures than the more advanced stages of pre-main sequence, where most of the original material has been incorporated to the young star (see Lada 1999).

Class 0 (André et al. 1993) and I (Adams et al. 1987; Lada 1987) sources are characterized by SEDs with peaks in the far-infrared and sub-millimeter, as a result of the emission of a cold dust collapsing envelope. These objects are the most deeply embedded and obscured. Once the collapse of the envelope ceases, the dusty disk can still produce substantial emission in the infrared. This part of the evolution gives rise to Class II and III sources (Adams et al. 1987; Lada 1987), whose SEDs are characterized by peaks in the optical and near-infrared, where stellar photospheric emission dominates. These objects correspond to T Tauri stars (CTTS and WTTS).

Based on the shapes of SEDs of observed infrared sources, Adams et al. (1987) defined the spectral index α between 2-25 μm as:

$$\alpha = \frac{d \log(\lambda F_\lambda)}{d \log(\lambda)} \quad (27)$$

where F_λ is the flux corresponding to wavelength λ . The different spectral indices computed in regions of star formation are interpreted as an evolutionary sequence, obtaining the following classification: $\alpha > 0$ for Class I sources, $0 > \alpha > -2$ for Class II sources, and $\alpha < -2$ for Class III sources.

The SEDs of the IRAS globules are shown in Figure 12. To calculate the spectral index we fitted a straight line using the least squares method to the points between 2.2 and 25 μm , with the requirement that these points have a determined uncertainty. Fluxes that are upper limits (shown as arrows in Figure 12) were not taken into account. Table 8 shows the name of the globule in column 1, the associated IRAS sources in column 2, the index α in column 3 and the corresponding spectral classification according to that index in column 4. It was possible to determine the spectral index for 8 of 13 IRAS sources, of which 6 correspond to Class I, one to Class II and one to Class III.

6.2. The BLT Diagram

A useful tool for studying the evolutionary state of a young object is the graph of the bolometric luminosity (L_{bol}) vs. bolometric temperature (T_{bol}) (BLT diagram). Myers & Ladd (1993) defined and used the BLT diagram to study the evolutionary state of YSOs in the Taurus-Auriga complex. T_{bol} is defined as the temperature of a blackbody which has the same mean frequency of the observed continuum spectrum. A main-sequence star whose

Table 8. Spectral Classification of YSOs in Bok Globules

Name	IRAS	α	Class ^a	L_{bol} (L_{\odot})	T_{bol} (K)	Class ^b
034	08250-5030	1.0	29	0
058	10471-6206	1.3	I	2.2	32	0
117	16029-4548	-1.0	II	4.2	742	II
121	16549-5030	0.6	227	I
	16554-5031	1.7	I	1.3	98	I
126	16009-3927	-2.5	III	37.6	2478	II
138	17159-4324	3.3	28	0
139	17172-4316	0.7	I	2.8	123	I
	17169-4314	1.9	90	I
140	17193-4319	1.5	I	1.9	35	0
	17195-4320	15.4	1676	II
148	17011-3613	1.6	I	1.6	31	0
149	17012-3603	1.1	I	1.5	39	0

^aSpectral classification according to index α

^bSpectral classification according to T_{bol}

spectrum is a blackbody has $T_{bol} = T_{eff}$. A pre-main sequence star with infrared excess has a wider and redder spectrum than a blackbody, and therefore $T_{bol} < T_{eff}$. An embedded infrared source is very reddened to have an optical measure of T_{eff} , its spectrum is much wider than a blackbody, and its T_{bol} is very small (< 500 K, Chen et al. 1995).

To derive the bolometric luminosity for the IRAS sources, we integrated their SEDs across the whole range in wavelengths:

$$L_{bol} = 4\pi D^2 \int_0^\infty F_\lambda d\lambda = 9.2\pi D^2 \int_0^\infty \lambda F_\lambda d\log\lambda. \quad (28)$$

In most cases, the lowest available wavelength to make the integration is the J band. As the SEDs for all the sources grow up as the wavelength increases (see Figure 12), we ignored the term between $\lambda = 0$ and the J band, which is very small compared to the total luminosity (see Baba et al. 2006). Therefore, the integration was divided into two parts:

$$L_{bol} = 9.2\pi D^2 \left(\int_{\lambda_1}^{\lambda_2} \lambda F_\lambda d\log\lambda + \int_{\lambda_2}^\infty \lambda F_\lambda d\log\lambda \right), \quad (29)$$

where $\lambda_1 = J$ and $\lambda_2 = 100 \mu\text{m}$, the longest available wavelength. To compute the second part of the integral, as we do not know the shape of the spectrum between λ_2 and infinity, we assumed that the SED is proportional to λ^{-1} (Wilking et al. 1989).

The bolometric temperature is defined by Myers & Ladd (1993) as:

$$T_{bol} \equiv \frac{\zeta(4)}{4\zeta(5)} \frac{h\bar{\nu}}{k_B} = 1.25 \times 10^{-11} \bar{\nu} \text{ (K Hz}^{-1}\text{)}, \quad (30)$$

where $\zeta(n)$ is the Riemann zeta function of argument n and the mean frequency $\bar{\nu}$ is the ratio of the first and zeroth moments of the source spectrum:

$$\bar{\nu} = \frac{\int_0^\infty \nu F_\nu d\nu}{\int_0^\infty F_\nu d\nu}. \quad (31)$$

Once we calculated these parameters, we constructed the BLT diagram. Chen et al. (1995) established a correlation between the temperature ranges in the BLT diagram and the evolutionary class of a YSO, getting as a result the following classification: $T_{bol} < 70$ K for Class 0, $70 \text{ K} < T_{bol} < 650$ K for Class I, $650 \text{ K} < T_{bol} < 2800$ K for Class II, and $T_{bol} > 2800$ K for Class III sources. The values of T_{bol} , L_{bol} and spectral classification according to this criterion are shown in columns 5, 6 and 7 of Table 8, respectively. Out of 13 IRAS

sources, 6 were classified as Class 0, 4 as Class I, and 3 as Class II. The BLT diagram is shown in Figure 13, where the solid line is the ZAMS from Siess et al. (2000) and the vertical dashed lines represent the intervals corresponding to different spectral classes.

The mean value of the Bonnor-Ebert stability parameter is ~ 5 for each spectral class, suggesting that there is no difference between the average value of the stability parameters of the cores and the spectral class of their associated IRAS sources.

7. BHR 138: A Collapsing Globule?

In this section, we will use the millimetric observations data of the ^{13}CO and C^{18}O molecules, in the rotational transition $J = 1 \rightarrow 0$, to study BHR 138 and BHR 149 (core A). Both globules are part of a survey of more than 30 condensations identified in Scorpius (Vilas-Boas et al. 2000). Among all these condensations, only BHR 138 presents a blue-asymmetric profile, while BHR 149 shows a typical profile observed in the others condensations. The presence of a blue-asymmetric profile in the spectrum of BHR 138 provides evidence of an eventual gravitational collapse. No spectral line data were available to study the other globules.

7.1. Reduction of the Spectra

The reduction of ^{13}CO and C^{18}O spectra was made with the spectral lines reduction program Drawspec⁶. The lines were adjusted with gaussians. In the case of BHR 138, the fitting was made with two independent gaussians. For more details about the reduction of the spectra and the derivation of the line parameters, see Vilas-Boas et al. (1994).

Figure 14 shows the ^{13}CO and C^{18}O spectra for BHR 138 and BHR 149. The histogram corresponds to the observed spectrum and the grey gaussians are the fitting made with Drawspec. For the ^{13}CO line in BHR 138, the resulting gaussian is the sum of the two thin gaussians. Table 9 shows the parameters extracted from the line fitting. Column 1 is the antenna temperature corrected from atmospheric attenuation, column 2 is the velocity of the line center, and column 3 is the FWHM of the line.

⁶<http://www.cv.nrao.edu/~hlistz>

7.2. Modelling of the ^{13}CO Line

Comparing the spectra of ^{13}CO for BHR 138 and BHR 149 in Figures 14 (a) and (b), respectively, we can see clearly the asymmetry in the line of BHR 138, while BHR 149 shows a perfectly symmetric line. The spectrum of BHR 138 does not presents two distinct peaks (see, e.g., Evans 1999), but do presents a typical profile of collapsing clouds denominated “red-shoulders” by Myers et al. (1996).

Given the blue-asymmetric profile shown by the ^{13}CO line in BHR 138, one of the fundamental questions is to know if this is really a profile indicative of collapse. One of the possibilities to explain that profile will be the superposition of distinct clouds in the line-of-sight or rotational effects of the clouds. Analysis of the field of the globule (Figure 2) shows a completely isolated object and the antenna beam contains only the globule. Similar situation occurs with BHR 149, which is also isolated and the profile does not suggests any asymmetry in the lines. Analysis of 30 globules in Scorpius also does not show profiles with asymmetries of the kind identified in BHR 138. According to Vilas-Boas et al. (2000), only 4 condensations of their sample observed in that region present contamination for superposition of clouds in the antenna beam. Generally, the components that contaminate the CO emission in that region have very wide line widths ($> 4 \text{ km s}^{-1}$) at different radial velocities.

Because the ^{13}CO and C^{18}O emissions are originated in the more external regions of the globules, with densities lesser than 10^5 cm^{-3} (e.g., Alves et al. 1999), we would also expect to identify that asymmetry in the C^{18}O line. Nonetheless, the signal-to-noise ratio for the spectrum of that molecule does not allow to identify a red-shifted component with sufficient accuracy. More greater integrations will be necessaries to improve the signal-to-noise ratio.

The first model, proposed by Myers et al. (1996), is called *two-layer* and consists of two collapsing gas layers, one approaching the other with a velocity of twice the infall velocity v_{in} . Each layer has a constant excitation temperature: the front layer, moving away from the observer, has a temperature T_f equal to the background temperature ($T_f = 2.7 \text{ K}$), while the rear layer, which is hotter, has a temperature T_r . Assuming that both layers have the same velocity dispersion σ and optical depth τ_0 at the line center, De Vries & Myers (2005) obtained the brightness temperature emerging from the spectral line:

$$\Delta T_B = J(T_r)(1 - e^{-\tau_r})e^{-\tau_f} + J(T_f)(e^{-\tau_f - \tau_r} - e^{-\tau_f}), \quad (32)$$

where $J(T) = T_0/[\exp(T_0/T) - 1]$, $T_0 = h\nu/k_B$, ν is the transition frequency, and τ_f and τ_r are the optical depth of the radiation coming from the front and rear layers, respectively:

$$\tau_f(v) = \tau_0 \exp \left[-(v - v_{LSR} - v_{in})^2 / 2\sigma^2 \right], \quad (33)$$

$$\tau_r(v) = \tau_0 \exp \left[-(v - v_{LSR} + v_{in})^2 / 2\sigma^2 \right], \quad (34)$$

where v_{LSR} is the line-of-sight velocity, assumed to be the same for both regions. Therefore, this model has five free parameters:

$$\tau_0, v_{in}, T_r, \sigma, v_{LSR}.$$

The second model, introduced in De Vries & Myers (2005), called *hill* model, consists of a dense core with a peak excitation temperature T_p at the center, and a temperature T_0 at the core edges. The $J(T)$ profile decreases linearly from $J(T_p)$ at the center to $J(T_0)$ at the edges. The optical depth is τ_C and the infall velocity is v_C . Assuming $T_0 = 2.7$ K, this model has five free parameters:

$$\tau_C, v_C, T_p, \sigma, v_{LSR}.$$

For a graphical representation and different variants of the models of De Vries & Myers (2005), see their Figure 1 and their Tables 1 and 2.

7.3. Modelling Results

To perform the fitting of the parameters for each model, we used a routine developed by De Vries & Myers (2005), obtained from the site of C. H. De Vries⁷. Starting values must be supplied to the program to find the best fitting parameters. Table 10 shows the results obtained with the *two-layer* model, and Table 11 shows the results corresponding to the *hill* model. The model that best fit the observational data for BHR 138, according to the χ^2 value, is the *two-layer* model. Figure 15 shows the fitting obtained with this model, where the grey curve represents the theoretical fit, which suggests a velocity collapse of 0.25 km s^{-1} . Considering that rotation was not taken into account, the derived collapse velocity should be seen as upper limit.

Possible rotational effects of the globules (Barranco & Goodman 1998) would be evaluated from maps of optically thin molecular transitions (e.g., N_2H^+). Studies of rotation

⁷http://cfa-www.harvard.edu/~cdevries/analytic_infall.html

Table 9. Observed Parameters of Spectral Lines

	T_A^* (K)	V_{LSR} (km s ⁻¹)	ΔV (km s ⁻¹)
BHR 138			
¹³ CO	2.57 ± 0.11	-7.62 ± 0.01	0.78 ± 0.03
	1.32 ± 0.10	-7.27 ± 0.04	2.18 ± 0.09
C ¹⁸ O	0.46 ± 0.05	-7.55 ± 0.05	0.82 ± 0.11
BHR 149			
¹³ CO	3.12 ± 0.03	1.11 ± 0.01	1.02 ± 0.01
C ¹⁸ O	0.31 ± 0.03	1.08 ± 0.05	1.01 ± 0.12

Table 10. Two-Layer Model Fitting for BHR 138

τ_0	v_{in} (km s ⁻¹)	T_r (K)	σ (km s ⁻¹)	v_{LSR} (km s ⁻¹)	χ^2
1.6	0.25	10.9	0.6	-6.9	1.2

Table 11. Hill Model Fitting for BHR 138

τ_C	v_C (km s ⁻¹)	T_p (K)	σ (km s ⁻¹)	v_{LSR} (km s ⁻¹)	χ^2
4.2	0.49	7.7	0.3	-7.1	3.8

in starless globules through the transition NH_3 (1,1) show maximum velocity gradients, due to rotation, of the order of $1.4 \text{ km s}^{-1} \text{ pc}^{-1}$ (Barranco & Goodman 1998; Swift et al. 2005), and a survey of 12 starless globules and 14 protostellar globules in N_2H^+ (Caselli et al. 2002) suggest typical velocity gradients of $2 \text{ km s}^{-1} \text{ pc}^{-1}$ in both kind of globules.

Adopting a mean velocity gradient due to rotation of $1.4 \text{ km s}^{-1} \text{ pc}^{-1}$ as being typical for Bok globules, it is possible that the collapse velocity derived for BHR 138 could be overestimated by 40% due to rotational effects that were not corrected in this work. Of the factors that would affect this conclusion, rotation seems to be the most relevant component. Taking that gradient and the size of BHR 138, rotation could be contaminating the spectrum with 0.14 km s^{-1} , assuming the angular momentum perpendicular to the line-of-sight. In that case, the collapse velocity would be $\sim 0.1 \text{ km s}^{-1}$.

In a sample of 53 starless cores observed in N_2H^+ , Lee et al. (2001) found collapse velocities of $\sim 0.1 \text{ km s}^{-1}$ using the *two-layer* model. Using observations of CS, Swift et al. (2006) obtained a collapse velocity of 0.15 km s^{-1} for the starless core L1551-MC with the *hill* model. Myers et al. (1996), utilizing the *two-layer* model, derived a collapse velocity of 0.35 km s^{-1} for the dense core L1251B, which harbors a protostar.

8. Summary

In this work, we studied a sample of 21 isolated Southern Bok globules selected among 169 globules catalogued by BHR. In this sample, 11 are starless and 10 have associated IRAS point sources. Employing the NICE method of Lada et al. (1994), we used the 2MASS PSC to construct visual extinction maps for the Bok globules with $20''$ resolution. This enabled us to detect dense cores and substructures embedded in the globules, which were modelled with Bonnor-Ebert spheres to derive their physical parameters and investigate their stability. Two methods were used to determine the spectral class of the IRAS sources associated to the globules. In addition, we searched for spectral lines observations data obtained toward these globules to explore whether they have or not evidence of collapse. We found observations of ^{13}CO and C^{18}O $J = 1-0$ lines toward two globules of the sample showing evidences of collapse in one of them. Distances were estimated to all these globules from plots of color excess versus distance. The main results of this paper are summarized as follows:

1. Dense cores were identified embedded in the globules, with mean volumetric densities greater than 10^4 cm^{-3} and masses between $\sim 1-4 M_\odot$.
2. We inferred distances to several globules different from that ones obtained by BHR in spite of using the same technique. Due to the uncertain nature of this method, in order

to improve the distance determination, we used smaller areas and a catalog containing information for approximately 10 times more stars than the catalog utilized by BHR.

3. We found that there is a large number of cores in the stable regime, followed by an abrupt decrease of cores in the unstable regime, but this decrease is steeper for IRAS globules than for starless. The globules that are in the stable state have a temperature of $T = 15 \pm 6$ K, while the globules that are in the critical and unstable states have a remarkably different temperature of $T = 10 \pm 3$ K.
4. We found that, according to the bolometric temperature, 6 IRAS sources are classified as Class 0, 4 as Class I, and 3 as Class II. The spectral index also produced similar results. No correlation was identified between the Bonnor-Ebert stability parameter of the condensations and the spectral class of the associated IRAS sources.
5. By means of the ^{13}CO J = 1–0 molecular line, we identified a blue-asymmetric line profile toward BHR 138. Using the *two-layer* collapse model, it was possible to estimate an infall speed of 0.25 km s^{-1} . However, taking into account possible rotational effects, this value could be as small as $\sim 0.1 \text{ km s}^{-1}$.

We are grateful to an anonymous referee for useful comments and suggestions that improved the manuscript. G. A. R. is grateful to a PCI-INPE/CNPq fellowship and a CAPES grant. This publication makes use of data products from the Two Micron All Sky Survey, which is a joint project of the University of Massachusetts and the Infrared Processing and Analysis Center, funded by the National Aeronautics and Space Administration and the National Science Foundation.

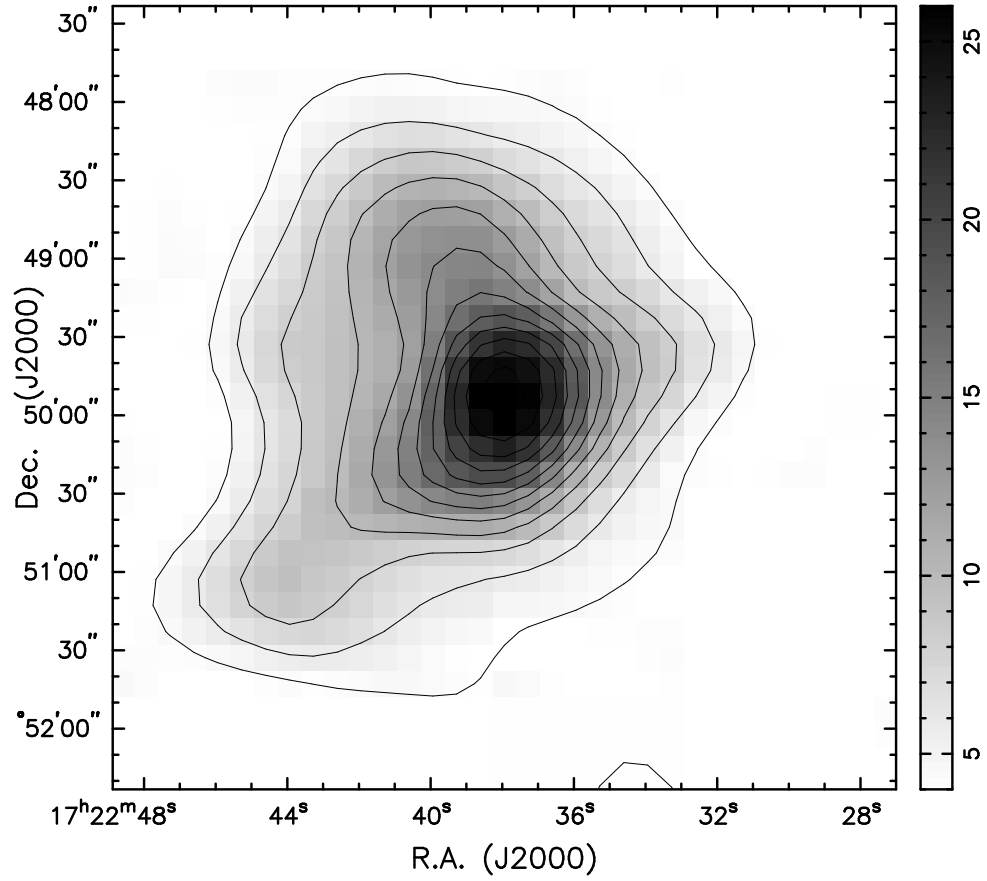


Fig. 1.— Extinction map for B68 constructed using 2MASS data with resolution $20''$. Contours start at $A_V = 4$ mag and increases in steps of 2 to 26 mag. Compare with the map of Alves et al. (2001).

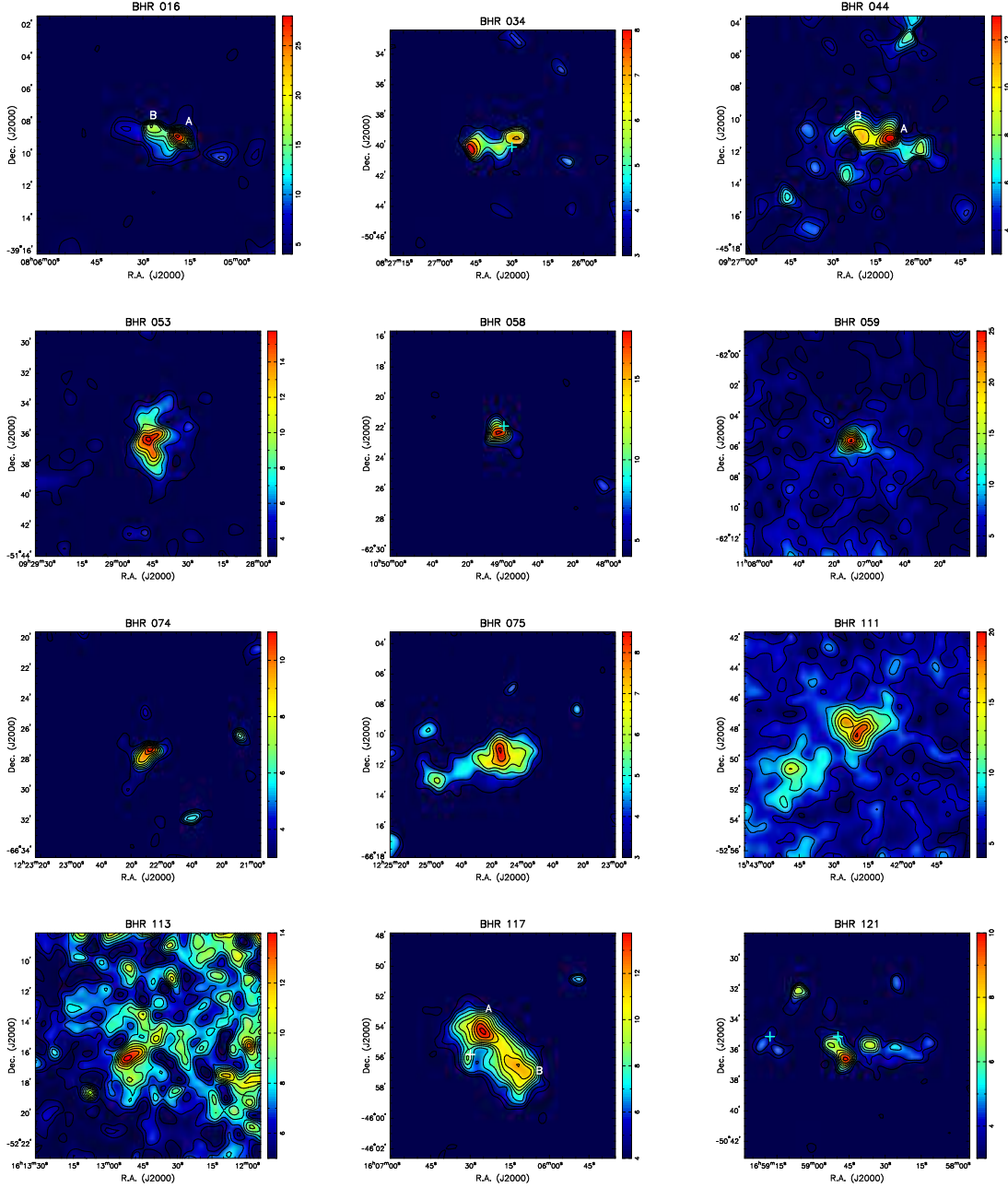


Fig. 2.— Visual extinction maps constructed with 2MASS data using the NICE method. Each map has $\sim 15' \times 15'$ and resolution $h = 20''$.

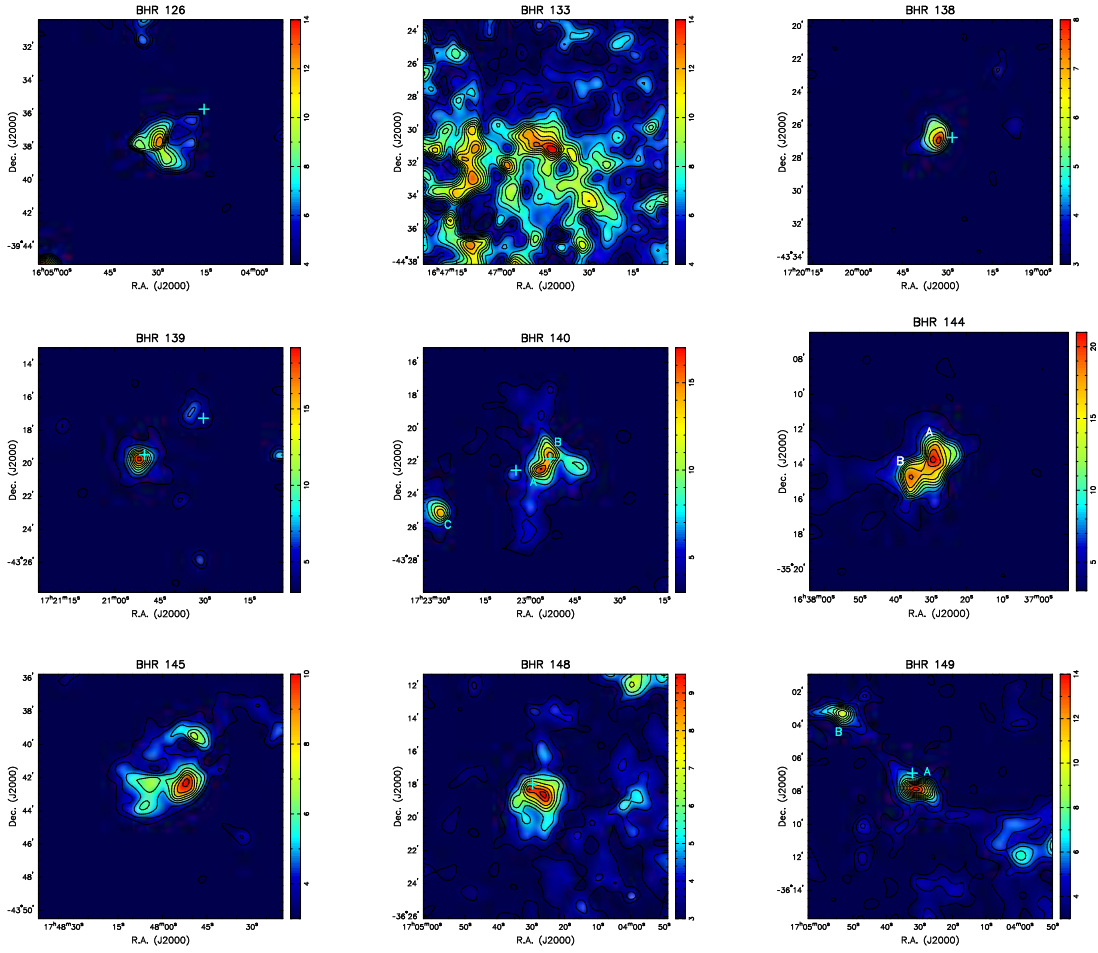


Fig. 2.— *continued.*

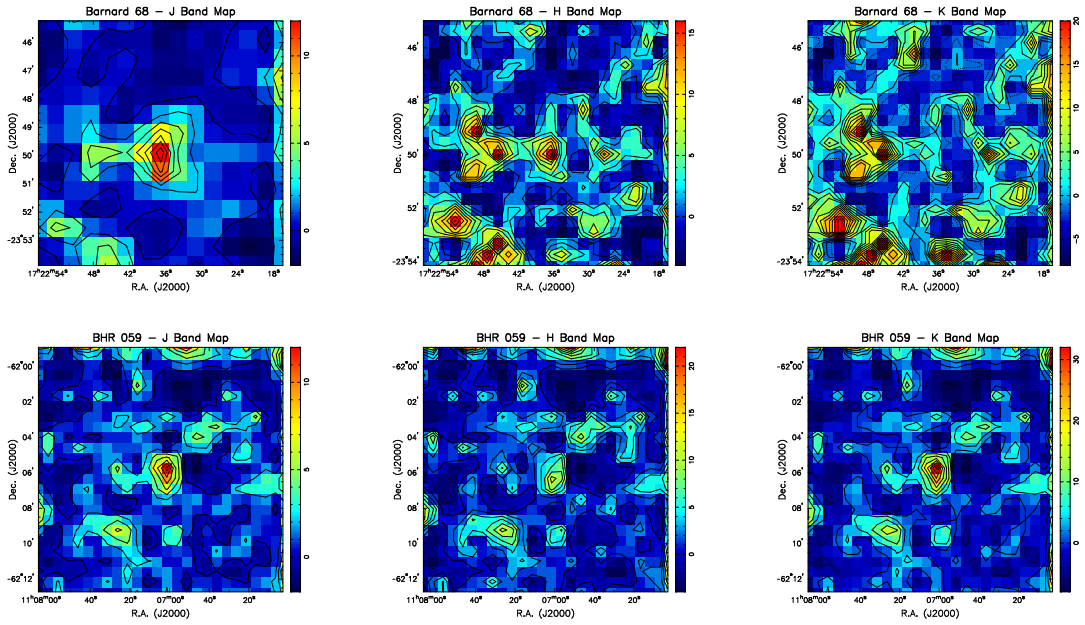


Fig. 3.— Visual extinction maps constructed with 2MASS data and the star counts method.

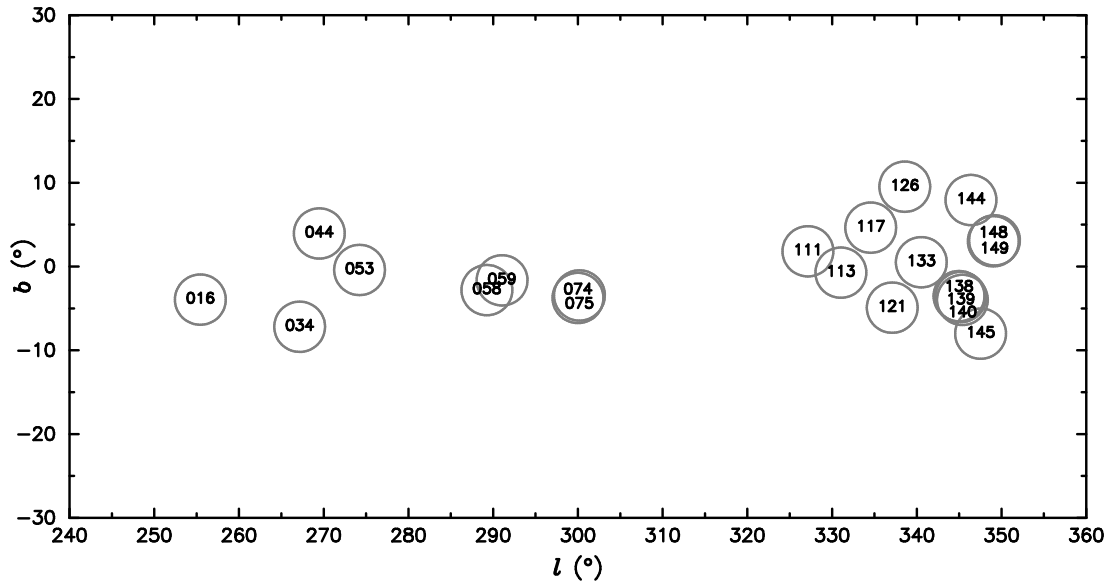


Fig. 4.— Galactic distribution of the Bok globules of our sample. The numbers are the names of the globules given in Table 1, and the circles represent the 3° regions used to search for stars in the SKY2000 catalog. In some cases (58-59, 74-75, 138-140, and 148-149), the same region was used.

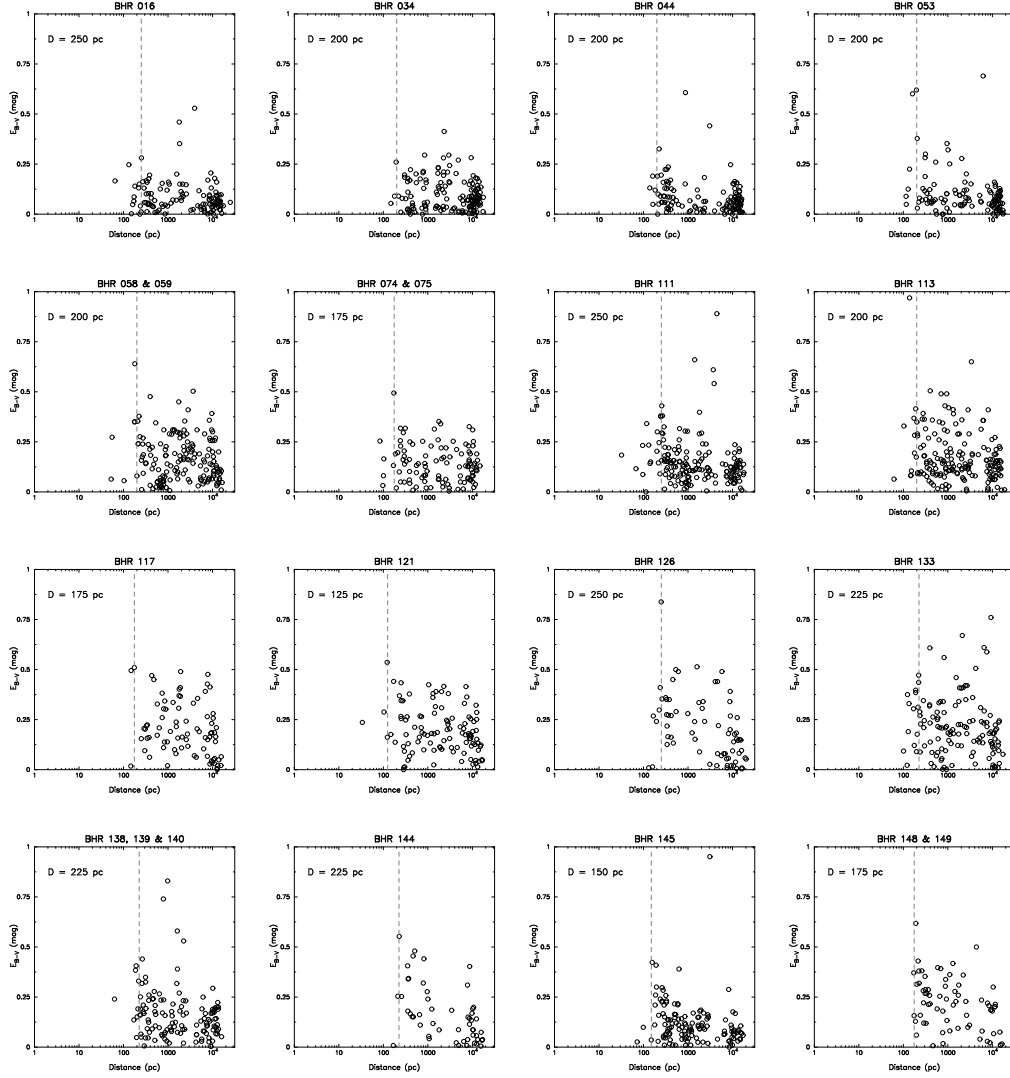


Fig. 5.— Color excess versus distance for stars in the neighborhood of each globule. The dashed vertical lines indicate the distances adopted in this work. In the upper left corner are given the distances estimated to the globules.

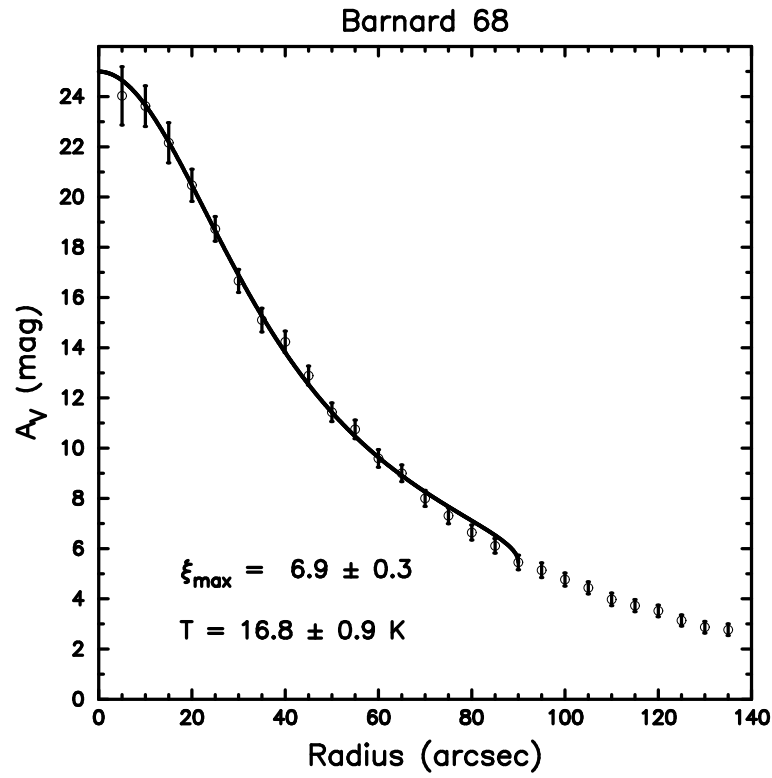


Fig. 6.— Azimuthally-averaged radial extinction profile for Barnard 68. The solid curve represents the Bonnor-Ebert theoretical profile fitting.

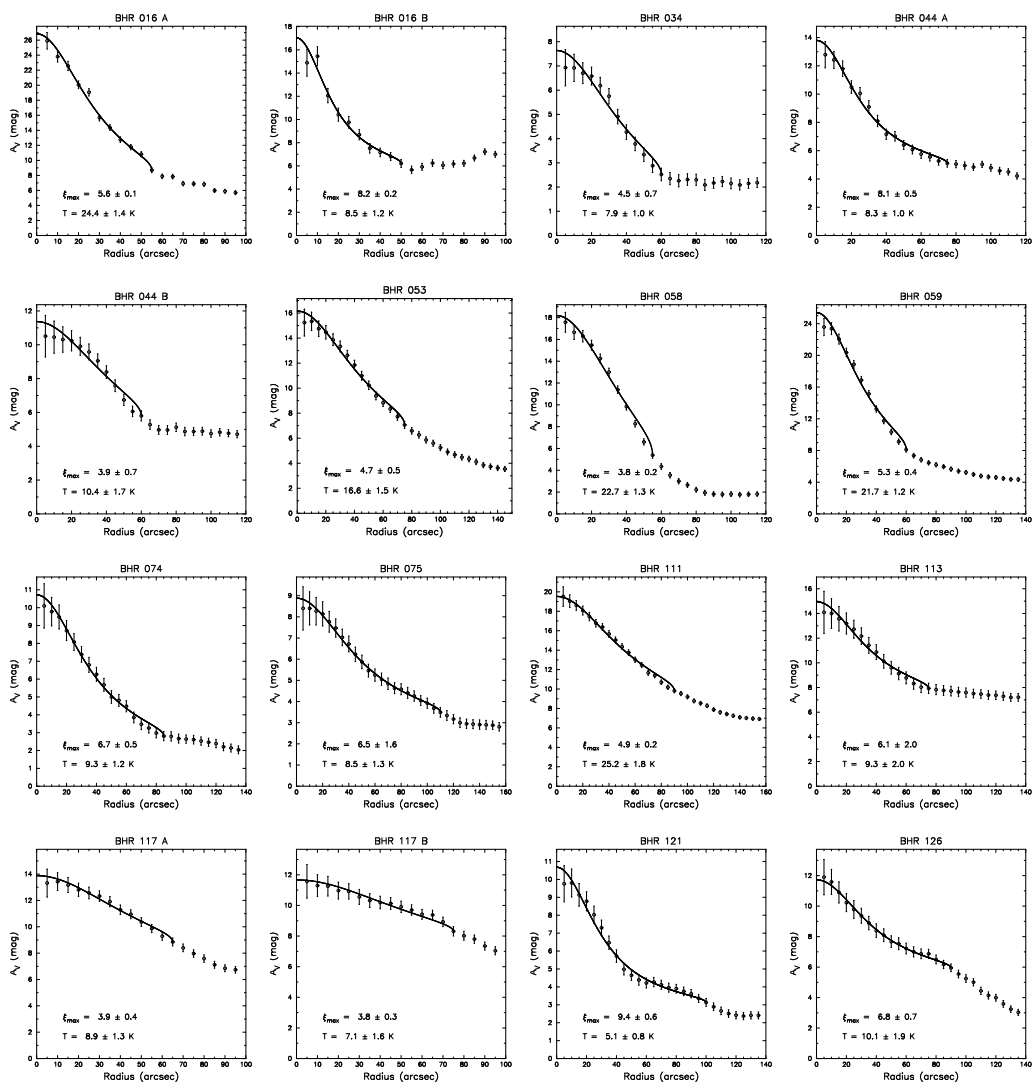


Fig. 7.— Azimuthally-averaged radial extinction profiles for dense cores in Bok globules. The solid curve superimposed on each observed profile represents the theoretical Bonnor-Ebert profile fitting.

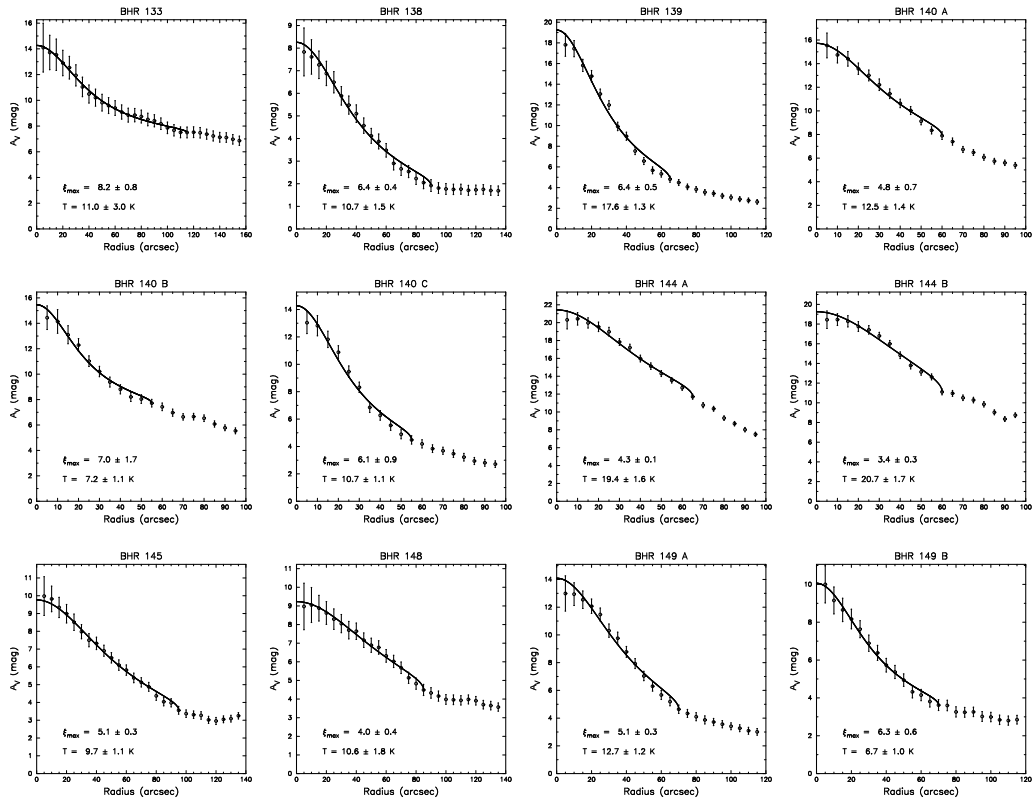


Fig. 7.— *continued.*

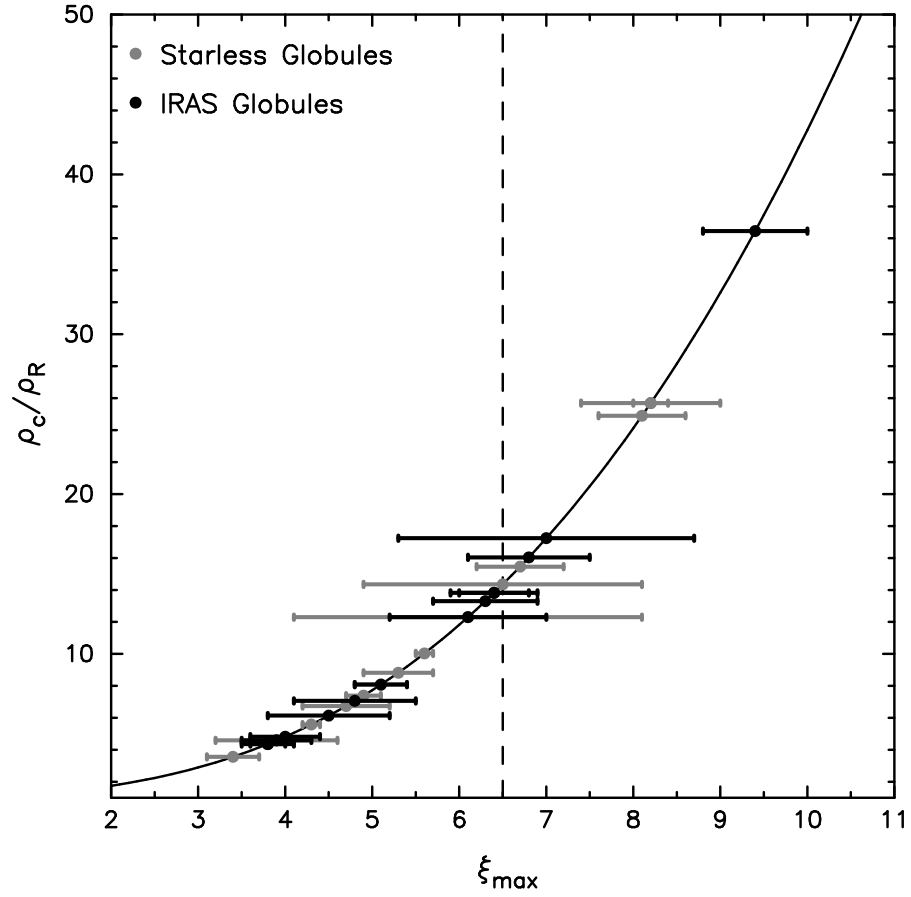


Fig. 8.— Relation between ξ_{max} and the center-to-edge density contrast for dense cores in Bok globules. Grey dots correspond to starless globules and black dots to IRAS globules. The vertical dashed line denotes the critical value $\xi_{max} = 6.5$.

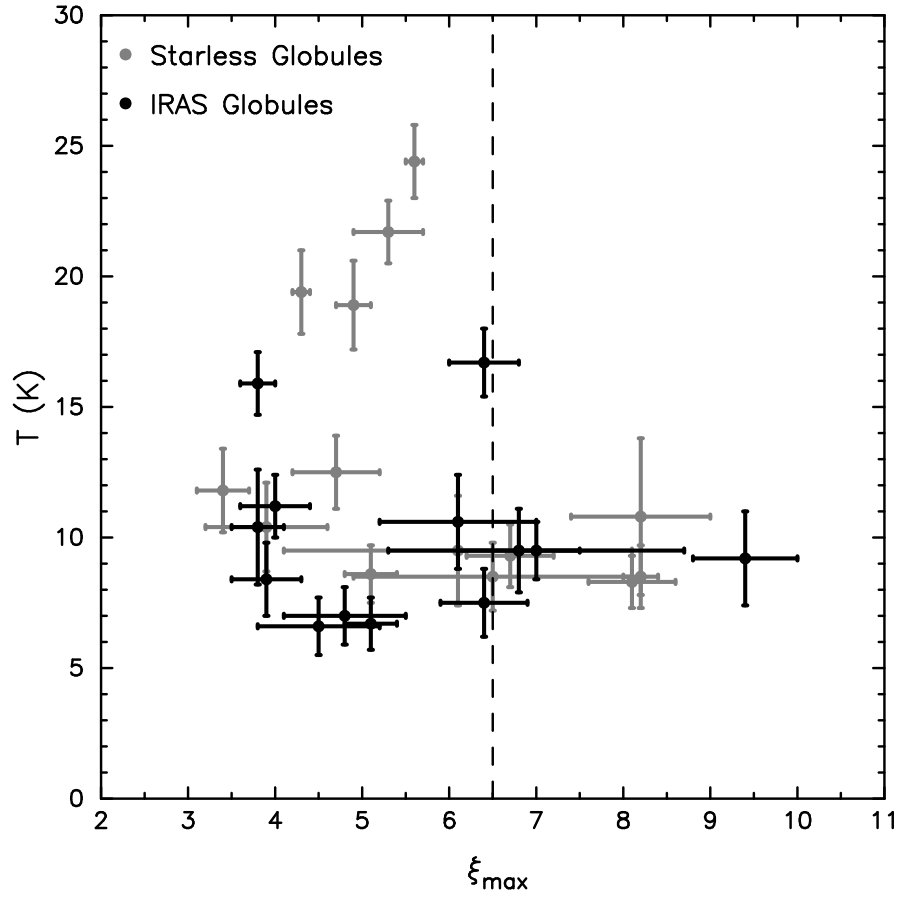


Fig. 9.— Relation between stability parameter and temperature for dense cores in Bok globules. The stable globules have $T = 15 \pm 6$ K and the critical plus unstable ones have $T = 10 \pm 3$ K. Grey dots correspond to starless globules and black dots to IRAS globules. The vertical dashed line denotes the critical value $\xi_{\max} = 6.5$.

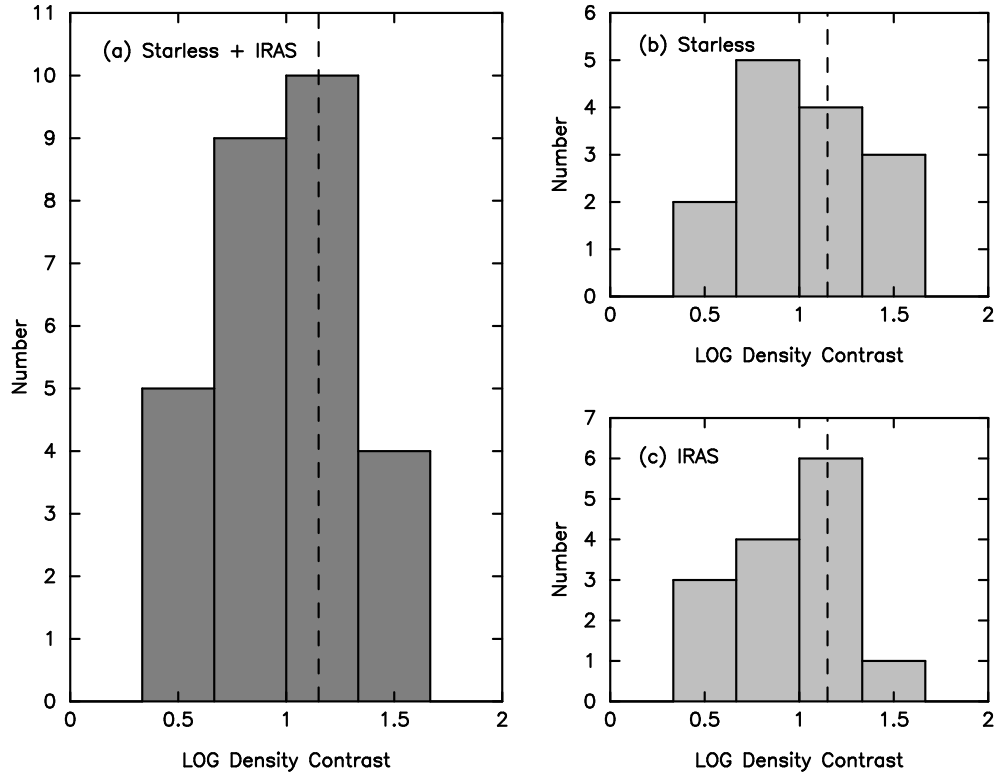


Fig. 10.— Histograms of the logarithmic density contrast for the whole sample of Bok globules (a), for starless globules (b), and for IRAS globules (c). The vertical dashed line denotes the critical value of the density contrast, $\rho_c/\rho_R = 14$.

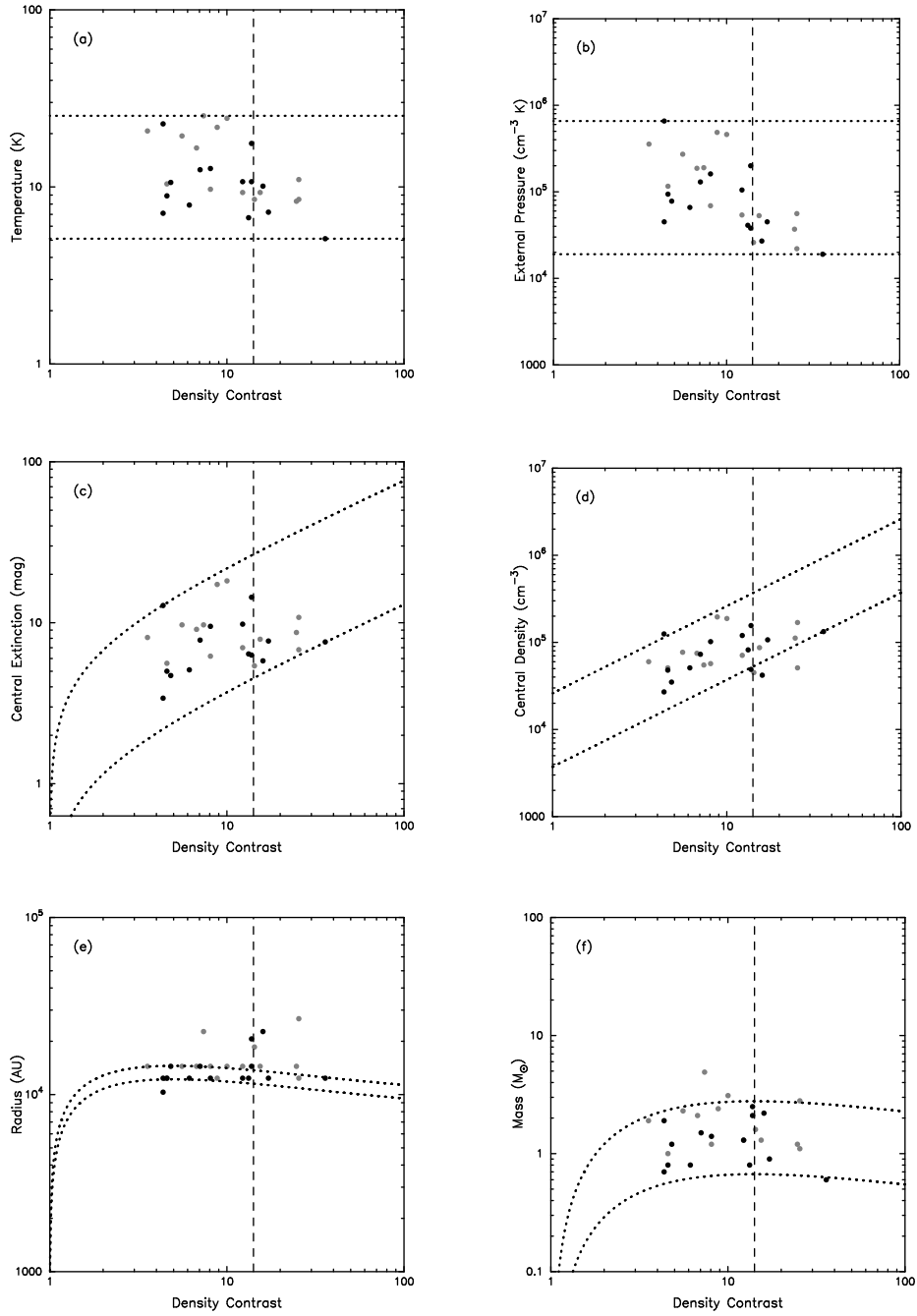


Fig. 11.— Correlations between density contrast and the parameters determined from the Bonnor-Ebert fitting of dense cores in Bok globules. (a)-(f) Plots for temperature, external pressure, central extinction, central density, radius and mass, respectively.

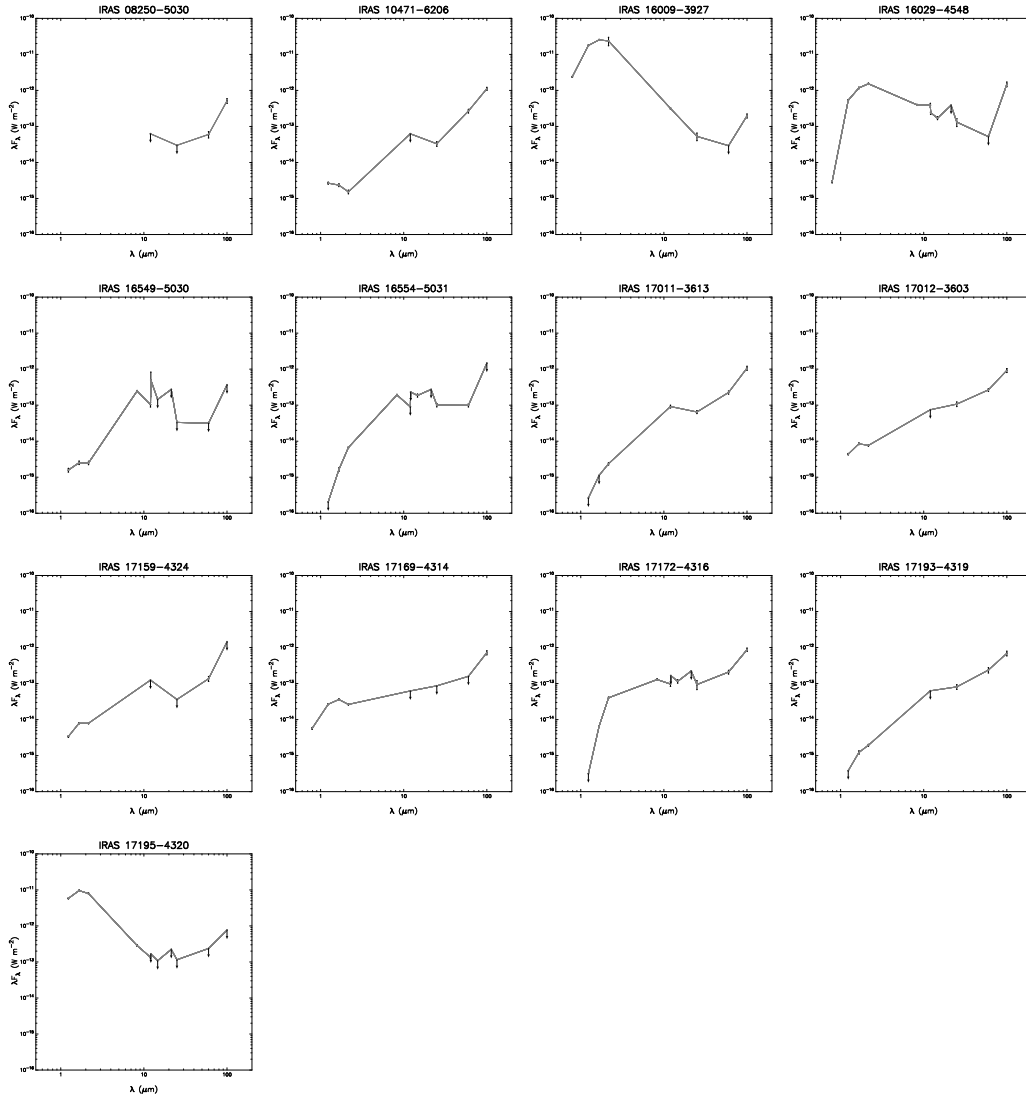


Fig. 12.— Spectral energy distributions for infrared IRAS sources associated to Bok globules.

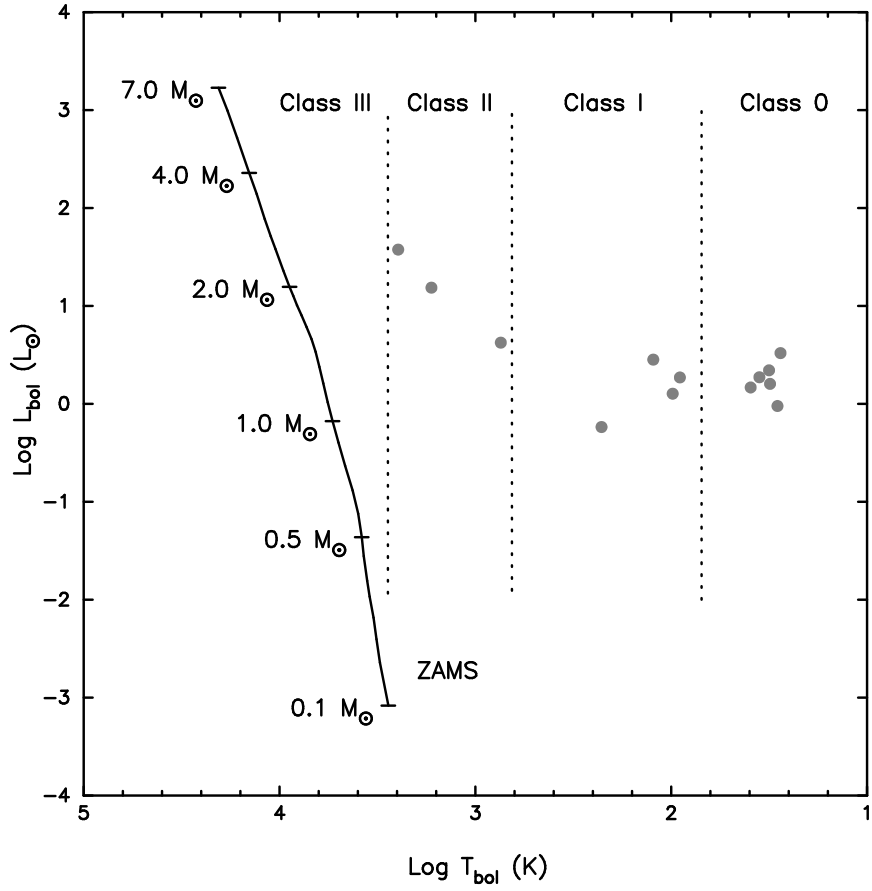


Fig. 13.— BLT diagram of infrared IRAS sources associated to Bok globules. The solid line indicates the ZAMS (Siess et al. 2000). The vertical dashed lines determine the limits of the different spectral classes (Chen et al. 1995).

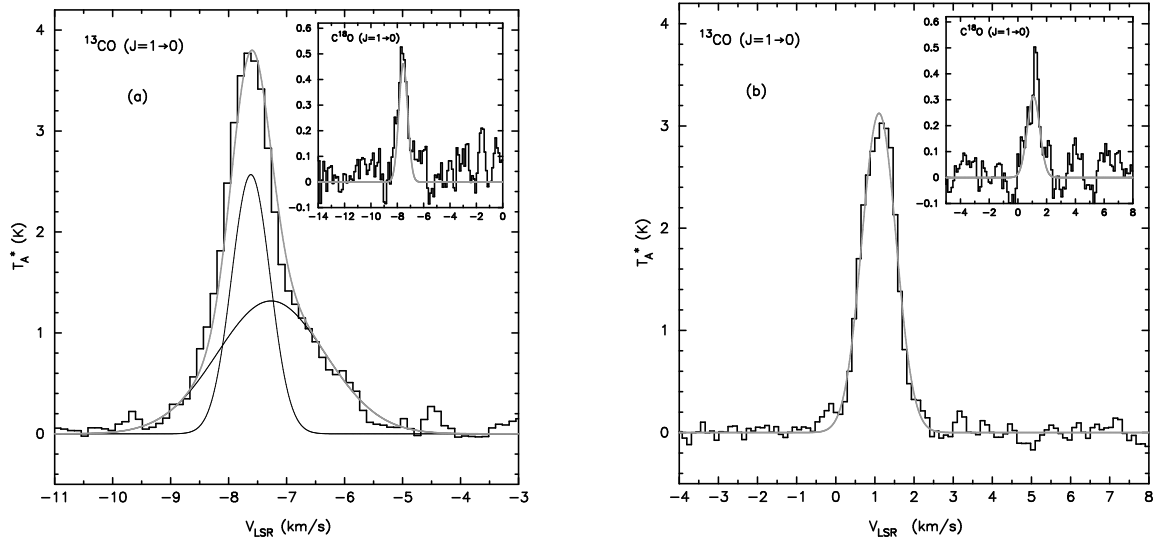


Fig. 14.— ^{13}CO and C^{18}O line profiles for (a) BHR 138 and (b) BHR 149.

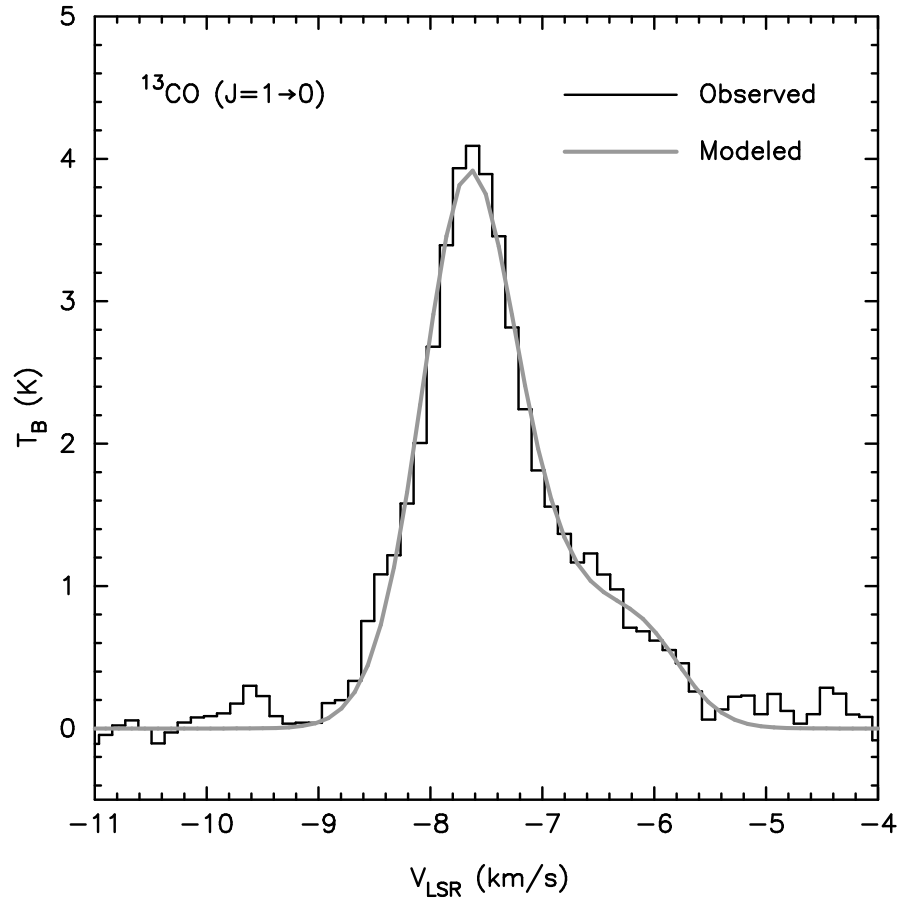


Fig. 15.— Modelling of the ^{13}CO line profile for BHR 138. The histogram represents the observational data and the grey curve corresponds to the *two-layer* fit model, which provides an infall velocity of 0.25 km s^{-1} .

REFERENCES

- Adams, F. C., Lada, C. J., & Shu, F. H. 1987, *ApJ*, 321, 788
- Alves, J. F., Lada, C. J., & Lada, E. A. 1999, *ApJ*, 515, 265
- . 2001, *Nature*, 409, 159
- André, P., Ward-Thompson, D., & Barsony, M. 1993, *ApJ*, 406, 122
- Baba, D., Sato, S., Nagashima, S., Kato, D., Haba, Y., et al. 2006, *AJ*, 132, 1692
- Barranco, J. A. & Goodman, A. A. 1998, *ApJ*, 504, 207
- Beichman, C. A., Myers, P. C., Emerson, J. P., Harris, S., Mathieu, R., Benson, P. J., & Jennings, R. E. 1986, *ApJ*, 307, 337
- Benson, P. J., & Myers, P. C. 1989, *ApJS*, 71, 89
- Bessell, M. S., & Brett, J. M. 1988, *PASP*, 100, 1134
- Bevington, P. R., & Robinson, D. K. 1992, *Data Reduction and Error Analysis for the Physical Sciences* (New York: McGraw-Hill)
- Bohlin, R. C., Savage, B. D., & Drake, J. F. 1978, *ApJ*, 224, 132
- Bok, B. J., & Bok, P. F. 1941, *The Milky Way* (Cambridge: Harvard University Press)
- Bok, B. B., & Reilly, E. F. 1947, *ApJ*, 105, 255
- Bonnor, W. B. 1956, *MNRAS*, 116, 351
- Bourke, T. L., Hyland, A. R., & Robinson, G. 1995a, *MNRAS*, 276, 1052 (BHR)
- Bourke, T. L., Hyland, A. R., Robinson, G., James, S. D., & Wright, C. M. 1995b, *MNRAS*, 276, 1067
- Cambrésy, L., Beichman, C. A., Jarrett, T. H., & Cutri, R. M. 2002, *A&A*, 123, 2559
- Caselli, P., Benson, P. J., Myers, P. C., & Tafalla, M. 2002, *ApJ*, 572, 238
- Chen, H., Myers, P. C., Ladd, E. F., & Wood, D. O. S. 1995, *ApJ*, 377, 392
- Clemens, D. P., & Barvainis, R. 1988, *ApJS*, 68, 257
- De Vries, C. H., & Myers, P. C. 2005, *ApJ*, 620, 800

- Dickman, R. L. 1978, *AJ*, 83, 363
- Dickman, R. L. & Clemens, D. P. 1983, *ApJ*, 271, 143
- Ebert, R. 1955, *Zeitschrift für Astrophysik*, 37, 217
- Epchtein, N., Deul, E., Derriere, S., Borsenberger, J., Egret, D., et al. 1999, *A&A*, 349, 236
- Evans, N. J. 1999, *ARA&A*, 37, 311
- Gredel, R., van Dishoeck, E. F., & Black, J. H. 1994, *A&A*, 285, 300
- Gregorio Hetem, J. C., Sanzovo, G. C., & Lépine, J. R. D. 1988, *A&AS*, 76, 347
- Hartley, M., Manchester, R. N., Smith, R. M., Tritton, S. B., & Goss, W. M. 1986, *A&A*, 63, 27
- Harvey, D. W. A., Wilner, D. J., Lada, C. J., Myers, P. C., Alves, J. F., & Chen, H. 2001, *ApJ*, 563, 903
- Harvey, D. W. A., Wilner, D. J., Lada, C. J., Myers, P. C., & Alves, J. F. 2003, *ApJ*, 598, 1112
- Hotzel, S., Harju, J., & Juvela, M. 2002a, *A&A*, 395, L5
- Hotzel, S., Harju, J., Juvela, M., Mattila, K., & Haikala, L. K. 2002b, *A&A*, 391, 275
- Huard, T. L., Myers, P. C., Murphy, D. C., Crews, L. J., Lada, C. J., et al. 2006, *ApJ*, 640, 401
- Kainulainen, J., Lehtinen, K., Väisänen, P., Bronfman, L., & Knude, J. 2007, *A&A*, 463, 1029
- Kandori, R., Nakajima, Y., Tamura, M., Tatematsu, K, Aikawa, Y., et al. 2005, *AJ*, 130, 2166
- Koornneef, J. 1983, *A&A*, 128, 84
- Lada, C. J. 1987, in *Star Forming Regions*, IAU Symposium 115, eds. M. Peimbert & J. Jugaku, 1
- Lada, C. J., Lada, E. A., Clemens, D. P. & Bally, J. 1994, *ApJ*, 429, 694
- Lada, C. J. 1999, in *The Origin of Stars and Planetary Systems*, eds. C. J. Lada & N. D. Kylafis (Dordrecht: Kluwer), 143

- Lada, C. J., Alves, J. F., & Lada, E. A. 1999, *ApJ*, 512, 250
- Lada, C. J., Bergin, E. A., Alves, J. F., & Huard, T. L. 2003, *ApJ*, 586, 286
- Lada, C. J., Huard, T. L., Crews, L. J., & Alves, J. F. 2004, *ApJ*, 610, 303
- Lai, S. -P., Velusamy, T., Langer, W. D., & Kuiper, T. B. H. 2003, *AJ*, 126, 311
- Lee, C. W., Myers, P. C., & Tafalla, M. 2001, *ApJS*, 136, 703
- Lombardi, M., & Alves, J. F. 2001, *A&A*, 377, 1023
- Maheswar, G., Manoj, P., & Bhatt, H. C. 2004, *MNRAS*, 355, 1272
- Mardones, D., Myers, P. C., Tafalla, M., Wilner, D. J., Bachiller, R., & Garay, G. 1997, *ApJ*, 489, 719
- Myers, J. R., Sande, C. B., Miller, A. C., Warren Jr., W. H., Tracewell, D. A., et al. 2002, *SKY2000 Catalog (V/109)*
- Myers, P. C., & Ladd, E. F. 1993, *ApJ*, 413, L47
- Myers, P. C., Mardones, D., Tafalla, M., Williams, J. P., & Wilner, D. J. 1996, *ApJ*, 465, L133
- Myers, P. C. 2005, *ApJ*, 623, 280
- Neugebauer, G., Habing, H. J., van Duinen, R., Aumann, H. H., Baud, B., et al. 1984, *ApJ*, 278, L1
- Nielbock, M. & Chini, R. 2005, *A&A*, 434, 585
- Price, S. D., Egan, M. P., Carey, S. J., Mizuno, D. R., & Kuchar, T. A. 2001, *AJ*, 121, 2819
- Racca, G., Gómez, M., & Kenyon, S. J. 2002, *AJ*, 124, 2178
- Rieke, G. H., & Lebofsky, M. J. 1985, *ApJ*, 288, 618
- Schmidt-Kaler, T. H. 1982, in *Landolt-Börnstein, New Series, Group VI, Vol. 2b, Stars and Star Clusters*, eds. K. Schaifers & H. H. Voigt (New York: Springer), 1
- Shu, F. H. 1977, *ApJ*, 214, 488
- Siess, L., Dufour, E., & Forestini, M. 2000, *A&A*, 358, 593

- Skrutskie, M. F., Cutri, R. M., Stiening, R., Weinberg, M. D., Schneider, S., et al. 2006, *AJ*, 131, 1163
- Swift, J. J., Welch, W. J., & Di Francesco, J. 2005, *ApJ*, 620, 823
- Swift, J. J., Welch, W. J., Di Francesco, J., & Stojimirović, I. 2006, *ApJ*, 637, 392
- Teixeira, P. S., Lada, C. J., & Alves, J. F. 2005, *ApJ*, 629, 276
- Vilas-Boas, J. W. S., Myers, P. C., & Fuller, G. A. 1994, *ApJ*, 433, 96
- . 2000, *ApJ*, 532, 1038
- Ward-Thompson, D., Scott, P. F., Hills, R. E., & André, P. 1994, *MNRAS*, 268, 276
- Ward-Thompson, D., Motte, F., & André, P. 1999, *MNRAS*, 305, 143
- Wilking, B. A., Lada, C. J., & Young, E. A. 1989, *ApJ*, 340, 823
- Wolf, M. 1923, *Astronomische Nachrichten*, 219, 109
- Zhou, S., Evans, N. J., Kömpe, C., & Walmsley, C. M. 1993, *ApJ*, 404, 232